THE UNIVERSITY
OF ADELAIDE
AUSTRALIA

Guiding Light in Low-Index Media via Multilayer Waveguides

by

Kristopher J. Rowland

Supervisors:
Prof. Tanya M. Monro
Dr Shahraam Afshar Vahid

A thesis submitted in fulfillment of the
degree of Doctor of Philosophy

in the
Faculty of Sciences
School of Chemistry & Physics

December 2010

Chapter 4

Liquid-Filled Bragg Fibres

CHAPTER 3 demonstrated how a 1D stratified binary dielectric medium can produce a rich 2D spectrum of photonic bandgaps. It was discussed how any waveguide whose cladding can be considered as such a layered medium will guide light with low loss within a low index core provided the light's $\tilde{n}(\lambda)$ (incident ray angle or effective mode index) lies within a bandgap of the cladding. Pertinent to the discussion of this chapter, Chapter 3 also showed how the bandgap edges shift significantly in frequency for varying $\tilde{n}$, *i.e.*, the bandgap edges are highly dispersive. This means that the low-loss transmission bands of the waveguide (the cladding bandgaps) can depend strongly upon the position of the guided modes' $\tilde{n}(\lambda)$ trajectory within the bandgaps (*e.g.*, Fig. 3.7).

This chapter is based on the results presented at the Conference on Lasers and Electro-Optics in Baltimore, Maryland, US, in 2009, oral presentation (K. J. Rowland), with a talk entitled *Spectral Properties of Liquid-Core Bragg Fibers* (authors: K. J. Rowland, S. Afshar V., A. Stolyarov, Y. Fink and T. M. Monro). The work was a collaboration with Prof. Yoel Fink and Alexander Stolyarov of the Massachusetts Institute of Technology (MIT) Photonic Bandgap Fibers and Devices Group, detailed further presently.

To elucidate this bandgap shifting mechanism further, note that $\tilde{n}(\lambda)$ of the core mode depends strongly upon the refractive index of the core, n_{core}. The regions of the bandgaps that the core modes intercept thus depend strongly upon n_{core}. By altering n_{core}, the transmission spectral peaks can thus be shifted in the direction of the intercept between the core mode and bandgap edges' $\tilde{n}(\lambda)$.

More precisely, since the bandgap structure extends from $\tilde{n} = 0 \rightarrow n_0$ (Chapter 3), and guided modes take values $\tilde{n} \leq n_{\text{core}}$, the value of n_{core} producing guided modes can exhibit effective index values of $1 \leq n_{\text{core}} \leq n_0$ (for dielectric filling materials, at least). Since the guided modes of large core waveguides typically exhibit $\tilde{n} \approx n_{\text{core}}$ (*e.g.*, Fig. 3.7 and § 2.3.1), upon filling the hollow waveguide's core with such materials, the guided modes' $\tilde{n}$ can also span this range of refractive indices: $1 \leq \tilde{n} \leq n_0$. Since the bandgap edges are dispersive, the frequency range enclosed by the intersection points of

the modes' $\tilde{n} = n_{\text{core}}$ with a given gap's edges will also be dispersive (thus exhibiting approximately the mean of the dispersion of the bandgap edges).

In this chapter, this core index dependent bandgap shifting effect is analysed experimentally (§ 4.2), with comparison to theory (§ 4.3). The experiment involves filling the core of a Bragg fibre with liquids of various refractive indices with the results compared to a Bloch wave bandgap model. The results are related to such applications as refractive index sensing. To begin, the some background history on the filling of hollow waveguides is discussed to motivate the results presented in the following section.

4.1 Motivation and History

One of the primary motivations of this experimental work was to demonstrate these effects and validate the associated concepts of the previous chapter and in particular the SPARROW model. There are currently at least two types of hollow-core waveguides that could demonstrate such behaviour upon changing the core index: Bragg fibres and Integrated-ARROWs. Each were discussed in detail in Chapters 1 and 3.

As has been mentioned in the previous chapters, the possibility of guiding light within low-index media by filling the hollow cores of such waveguides has potential applications in sensing [19], waveguide lasers [30], particle guidance [27, 29], and nonlinear optics [133].

Cox et al. [67] demonstrated how by filling the hollow core of an average-index Bragg fibre (Chapter 1) with water, the transmission can be shifted by hundreds of nm. However, the cladding of an average-index Bragg fibre consists of rings of holes, whereas the cladding of the more conventional Bragg fibre considered here consists of layered solid dielectrics. The work of Ref. [67] relied on filling the cladding holes as well as the hollow core, and only with one liquid. The case here is quite different in that the fibre structure is fundamentally different (solid cladding), the cladding indices are much higher than core indices considered, the cladding properties stay the same upon filling, and multiple liquids are used.

More research into this type of transmission spectrum shifting with respect to refractive index has been studied using an I-ARROW platform. Bernini et al. [58] theoretically analysed the behaviour of an I-ARROW in which the second of two layers of the waveguide consisted of a liquid channel; by altering the refractive index of the liquid in the layer, the high-loss regions of core-guided light could be tuned. Closer to the case at hand, the work of Campopiano et al. [59] demonstrates experimentally a similar concept but by filling a hollow-core I-ARROW with various liquids. The results showed how the

high-loss features of the transmission spectrum shift with the altered core index with a sensitivity of ≈ 555.55 nm/RIU (RIU: refractive index unit).

The great difference of the latter work with the results shown here is that the guidance of the waveguide used was closer to an antiresonance regime than a bandgap regime. The I-ARROW of [59] employed only 2 layers, whereas the Bragg fibre used here has many more. As per the bandgap evolution discussion of § 3.5.3, adding more layers to the structure makes the band structure more well-defined; this is the reason why the low-loss regions are a better feature to exploit for the few-layer case whereas, as will be shown here, the transmission peaks of the many-layer Bragg fibre are well-defined implying the high, not low, transmission features should be exploited for a sensing architecture since they are better defined.

In short, this chapter explicitly demonstrates the transmission band shifting effect within a Bragg fibre by filling it with a range of transparent liquids. Section 4.2 presents the experimental results of systematically filling a Bragg fibre with liquids of various refractive indices and measuring the resultant transmission spectrum. Section 4.3 then compares these results with what is expected from theoretical considerations.

To the best of my knowledge, prior to this work, such transmission spectrum shifting by systematically filling the hollow-core of a Bragg fibre had not been demonstrated. Indeed, it seems to not have been demonstrated for any hollow-core waveguide within the bandgap regime (many layers). With the highlighting of this Bragg fibre filling technique for refractive index sensing in the work of Skorobogatiy et al. [19] (which unfortunately overlooked the results I presented in [55]), it is clear that this platform holds some promise for applications to biological and chemical sensing, fibre lasers and nonlinear optics.

4.2 Experiment—Liquid Filling and Transmission Spectra

The Bragg fibre used for this work was very similar to that discussed in [42]. Collaboration with the MIT Photonic Bandgap Fibers and Devices Group was sought, as they are leaders in the area of Bragg fibre fabrication, with Prof. Yoel Fink (the group leader) being an author of most of the publications relating to Bragg fibre fabrication and demonstration mentioned in Chapter 1 (*e.g.*, [41, 42]—see Table 1.1 for more). With this collaboration, several samples of a particular Bragg fibre were made available. The particular fibre used, however, instead of guiding light in the near- to mid- infra-red when empty (like most reported hollow-core Bragg fibres to date), guided close to the long-λ edge of the visible spectrum at $\lambda \approx 700$ nm. 15 cm long samples of this fibre

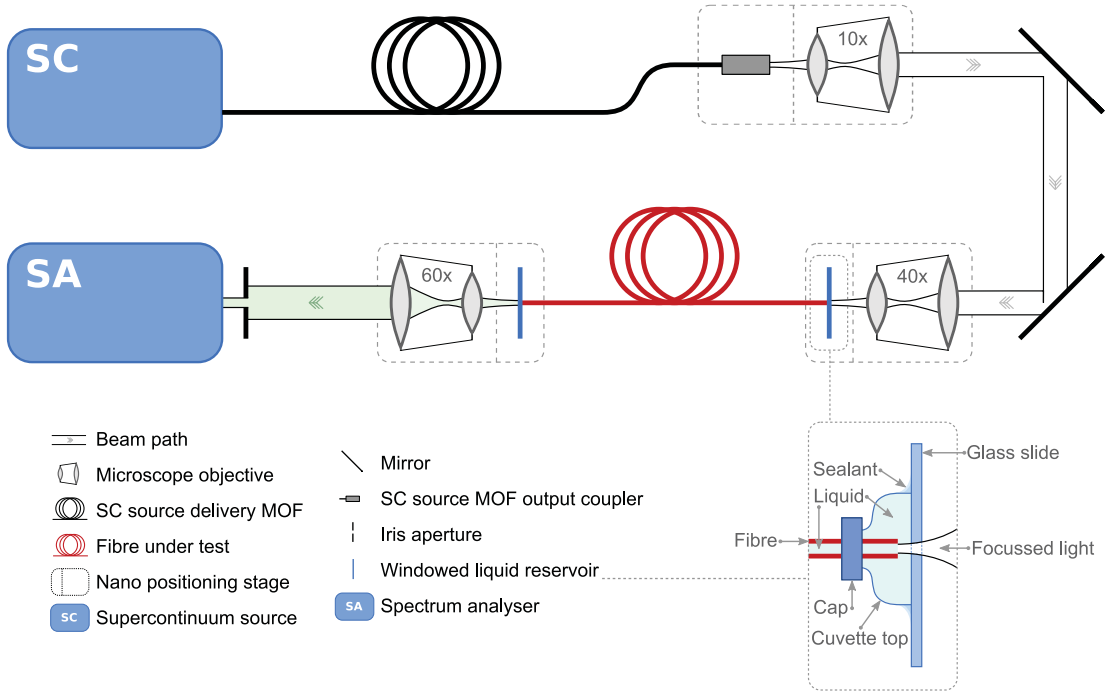

FIGURE 4.1: A schematic of the Bragg fibre filling and spectral measurement configuration. All optical components are labeled in the legend at the bottom of the figure. The light beam exiting the fibre is (arbitrarily) colored to represent the spectral filtering effect upon the white light due to the cladding structure. Each (cleaved) end of the Bragg fibre is hermetically sealed within its own liquid-filled windowed cell, as shown in the zoom-in region in the bottom right of the figure.

were used in the following tests. The hollow core was 330 μm in diameter, surrounded by a periodic cladding of concentric rings with 9 pairs of layers consisting of Arsenic Trisulphide (As_2S_3) chalcogenide glass and Poly-ether Imide (PEI) polymer of approximate thicknesses 76 nm and 124 nm, respectively. The cladding was terminated by a thick jacket of PEI producing a total outer diameter (OD) of 585 μm. The first and final As_2S_3 layers of the cladding were half-thickness (40 nm) in an attempt to minimise guided surface states (which, through inter-mode coupling, can introduce loss peaks in the core-modes' transmission spectra). Importantly, in the regimes of interest here, As_2S_3 and PEI have non-negligible material dispersion. This is an important point for Section 4.3.

In order to fill the fibre and measure the transmitted spectra, a hermetically sealed filling apparatus (Fig. 4.1) was employed: each end of the fibre is pierced though the rubber membrane of a sealed, windowed, cell. This technique was conceived of and custom-made for this application. The cells were hand-made, each consisting of the top of a laboratory grade capped cuvette and a microscope slide. To make such a cell, the top of a cuvette (to which a sealed screw-cap with a penetrable rubber membrane can be fastened) is cut from the cuvette body by carefully sawing it off with a glass-cutting saw.

The open (cut) side of the cuvette top is then placed against a clean microscope slide and sealed to it using a silicon based sealant, providing both a hermetic seal and sufficient mechanical stability [1]. This construction forms a the hermetically sealed windowed cell. The fibre under test can then be inserted into a hollow needle which is subsequently pierced through the rubber membrane of the screw-cap. The needle is then removed, sealing the membrane about the outside of the fibre. With both ends of the fibre sealed within these cells, light can be easily in- and out-coupled from the fibre via the cell windows formed by the microscope slides.

To fill the fibre, the membrane of one cell was pierced with a hollow needle, allowing the empty cell to be filled with a liquid under pressure. In order to prevent over pressurisation of the cells, a second hollow needle was inserted into the second cell's membrane prior to filling the first with the liquid sample. As the first cell was filled, the end of the fibre became immersed, after which the liquid was forced down the length of the fibre and into the second cell, displacing the air. Once the fibre and each cell were filled, the needles could be removed, leaving the fibre filled with, and suspended in, the liquid of interest. The existence of the cell windows makes coupling from free space, through the liquid reservoir, and into the fibre, an almost trivial affair, avoiding optical issues that could occur were menisci or bubbles to exist within the optical path.

The light source used as an input to the fibre was a fibre-based supercontinuum white-light source (a Koheras SuperK$^{\mathrm{TM}}$ Compact). A supercontinuum source such as this produces white light with a broader, flatter, spectrum at a much greater brightness than conventional sources, such as a filament globe, say. The supercontinuum itself is produced from the mutual interaction of many nonlinear optical effects such as self-phase modulation, cross-phase modulation, stimulated Raman scattering, and four-wave mixing, and hence are typically most efficient to excite in nonlinear fibre-based devices [204].

The liquids used to fill the fibre were 'Immersion Liquids' from the Cargille^{TM} with refractive indices 1.4019, 1.4620 and 1.5780 (all standardised at a wavelength of $\lambda =$ 589.3 nm and at a temperature of $25°C$). While the precise chemical composition of the liquids is not readily available for commercial reasons, they are thought to be organic solvents in various concentrations. All liquids used were transparent over the entire visible range so that, compared to the waveguide losses, the liquid material losses were negligible over the considered spectrum. According to the product data, the chromatic dispersion of the liquids was negligible (flat) compared to the dispersive properties of the fibre materials, modes and bandgap edges.

[1] The silicon based sealant appeared to be sufficiently chemically stable when in contact with all liquids used for the filling experiments.

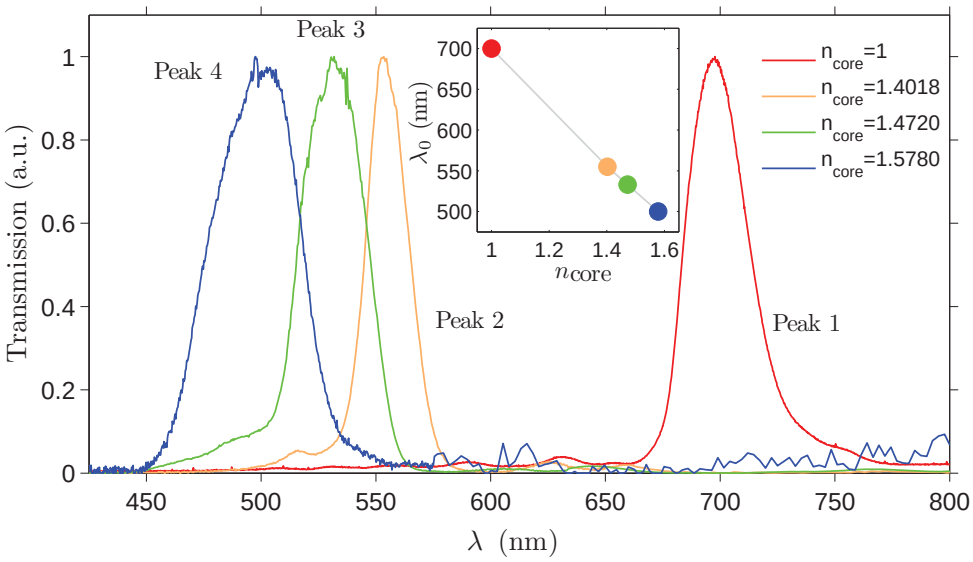

FIGURE 4.2: Experimentally measured transmission spectra from the filled and unfilled Bragg fibre, as shown in Fig. 4.1. Peak 1 corresponds to a non-filled (empty) fibre where $n_{\text{core}} = 1$ and peaks 2, 3, and 4 (right to left) correspond to a liquid filled core of refractive indices $n_{\text{liquid}} = 1.4018, 1.4720, \text{and} 1.5780$, respectively. Each spectrum is normalised to its own maximum value, *i.e.*, no relative loss information is contained in this representation. The inset figure represents spectral positions of the peak maxima against the filling refractive index—the trend is almost linear, owing to the property of the material dispersion 'straightening out' the bandgaps, as per § 4.3.

The light transmitted through the fibre was subsequently free-space coupled into an optical spectrum analyser (OSA), with spectral resolution $\delta\lambda = 0.05$ nm. Each spectral trace of the output light was point-averaged over 200 samples to reduce the signal to noise ratio due to low power throughput (depending on the bandgap regime accessed) and environmental influences, such as potential convection current in the liquid reservoir.

Fig. 4.2 shows the measured transmission spectra of the Bragg fibre when empty, $n_{\text{core}} = 1$ (Peak 1, Fig. 4.2), and when filled with each liquid, $n_{\text{core}} = 1.4018, 1.4720, 1.5780$ (Peaks 2 through 4, respectively, Fig. 4.2). There is a clear trend followed by the set of peaks: as the core index increases the wavelength monotonically decreases, covering almost the entire visible spectrum; peaks 1 to 4 (Fig. 4.2) have maxima at wavelengths of $\lambda_0 = 700$ nm, 555 nm, 533 nm and 500 nm, respectively. Also, the peak width appears to initially decrease and then increase again: peaks 1 to 4 have widths at half-maximum of 30 nm, 21 nm, 33 nm and 40 nm, respectively. This behavior coincides with what is qualitatively expected of the fundamental TM bandgap, discussed presently. These results are summarised in Table 4.1.

In general, the shifting, and hence sensitivity, of the transmission peaks with respect to n_{core} is not linear due to the dispersive properties of the band edges. Here, however, as will be shown in § 4.3, the dispersion of the layer materials themselves has the

Peak Number	n_{core}	$\lambda_0(nm)$	$\Delta\lambda_{\text{FWHM}}(nm)$	**Colour**
1	$n = 1$ (empty)	700 nm	30 nm	Dark Red
2	$n = 1.4018$	555 nm	21 nm	Yellow
3	$n = 1.4720$	533 nm	33 nm	Green
4	$n = 1.5780$	500 nm	40 nm	Green-Blue

TABLE 4.1: Summary of the filled Bragg fibre transmission peaks.

effect of 'straightening out' the band edges; this explains why the shifting of the peaks follows an approximately linear trend as shown in the inset of Fig. 4.2. Given this, the average shifting of the transmission peaks with core index here corresponds to an average sensitivity of $\partial\lambda_0/\partial n_{\text{core}} \approx 330$ nm/RIU. This sensitivity value is comparable with the I-ARROW refractive index sensors architecture of Ref. [59] discussed above. Indeed, this should probably be expected owing to the similarities between the bandgap and antiresonance regimes discussed in the previous chapter; the dispersive features of the antiresonance (SPARROW) and bandgap edges are quite similar, so that the sensitivity of the intercept of the core modes with these antiresonance or bandgap features is also similar. This result indicates that waveguides like the Bragg fibre indeed do hold promise for applications to refractive index sensing via the exploitation of cladding resonances (again, as suggested in Ref. [19] after I had performed these experiments and reported and analysed them in Ref. [55]).

4.3 Comparison with Theory

As discussed in Chapters 2 and 3, the cladding of a Bragg fibre can be approximated as a planar Bragg stack with the cladding bandgaps obtained from a Bloch-wave analysis. However, such analyses typically assume the cladding layer indices are constant. In the regimes considered here, it is important to explicitly include any material dispersion in the analysis for any meaningful comparison with experimental results. Figure 4.3 shows how the real part of the refractive index varies with wavelength (*i.e.*, the material dispersion) for the individual cladding layer materials used for the considered fibre (As_2S_3 and PEI). The curves are actually polynomial interpolation functions of thousands of experimentally measured data points (measured using a precise ellipsometric technique conducted by the MIT group).

In order to incorporate material dispersion into the Bloch analysis, the Bloch wave existence condition, $|\text{Re}(M_{11})| \leq 1$ from Eq. A.153, is evaluated using the continuously interpolated forms (8^{th}-order Gaussian series fits) of $n_{\text{As}_2\text{S}_3}(\lambda)$ and $n_{\text{PEI}}(\lambda)$, Fig. 4.3;

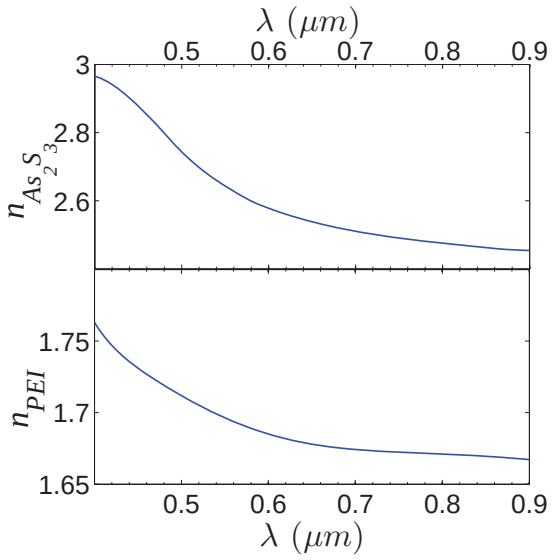

FIGURE 4.3: Material dispersion data for the materials constituting the Bragg fibre layers: As_2S_3 (top) and PEI (bottom). The curves used are actually 8^{th}-order Gaussian series fits to measured ellipsometric data points.

a function of the form $\sum_{n=0}^{8} e^{(x-a_n)^n/b_n}$ is optimised over a_n and b_n to fit the experimental refractive index data to within a 95% confidence interval. The results are two continuous interpolation functions $n_{\text{As}_2\text{S}_3}(\lambda)$ and $n_{\text{PEI}}(\lambda)$; the datapoints are practically indistinguishable from these curves when plotted as per Fig. 4.3. Note that the Gaussian fit was used instead of a more conventional *Sellmeier* fit (a series of inverse powers of wavelength) for reasons of convenience (a fitting routine was readily available for the Gaussian series).

Figure 4.4 shows calculated bandgap spectra when material dispersion is considered (bottom) and neglected (top); in the neglected material dispersion version I somewhat arbitrarily take $n_{\text{As}_2\text{S}_3} = n_{\text{As}_2\text{S}_3}(\lambda)|_{\lambda=700\text{nm}}$ and $n_{\text{PEI}} = n_{\text{PEI}}(\lambda)|_{\lambda=700\text{nm}}$. The bandgap spectrum neglecting material dispersion (Fig. 4.4, top) demonstrates how the bandgaps tend to flatten out as the wavelengths decreases. This behaviour can be explained using the SPARROW model (Chapter 3), in which the bandgap structure tends to follow the trajectories of the individual modes that would exist within the cladding layers were they isolated from the stack. The fundamental high-index SPARROW mode ($\tilde{n}_{m_1}$—the As_2S_3 layer since $n_{\text{PEI}} < n_{\text{As}_2\text{S}_3}\ \forall\lambda$) is dominant here, explaining why TE gap is open from below 1 to the lowest layer index within the wavelength range of interest; *i.e.*, the $\tilde{n}_{m_1=0}$ SPARROW mode curve never crosses the $\tilde{n}_{m_1=1}$ curve.

The high-index modes asymptotically approach the high layer index as λ decreases: $\tilde{n}_{m_1}(\lambda) \to n_1 = n_{\text{As}_2\text{S}_3}$ as $\lambda \to 0$. Since $n_{\text{As}_2\text{S}_3}(\lambda)$ and $n_{\text{PEI}}(\lambda)$ tend to increase as λ decreases (Fig. 4.3), the effect of incorporating material dispersion into the Bloch analysis is to 'straighten out' the bandgap edges; the increasing material indices tend to

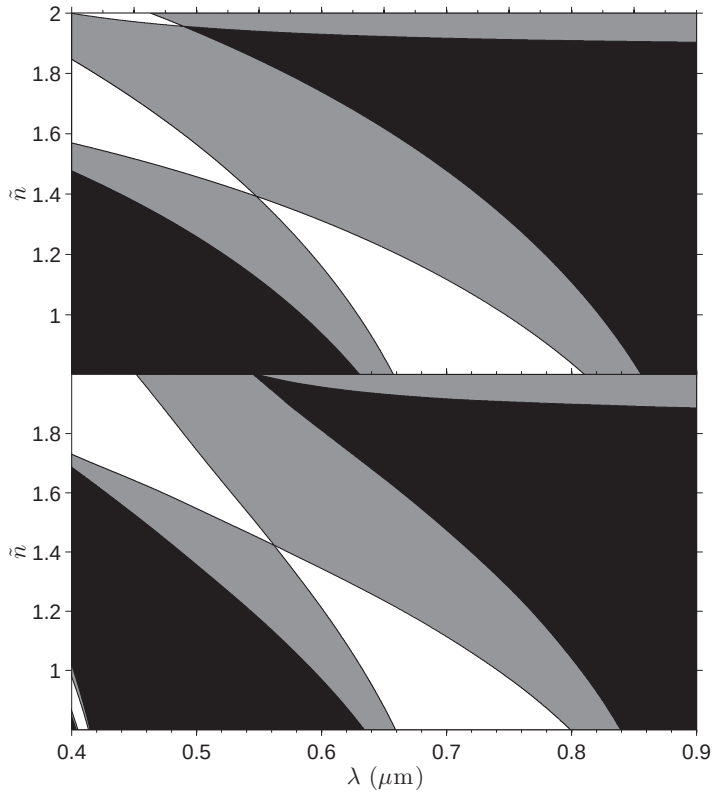

FIGURE 4.4: *Top*: the fundamental bandgap of the used Bragg fibre, *neglecting* material dispersion of the constituent layers. *Bottom*: the same bandgap spectrum with material dispersion (Fig. 4.3) included.

increase the effective mode index ($\tilde{n}_{m_1}$ and $\tilde{n}_{m_0}$ if considering the SPARROW picture). In other words, the asymptotes the SPARROW curves tend towards increase in value for lower wavelengths, straightening out the dispersion curves (similarly considerations would apply for the Bloch modes defining the band edges). Figure 4.4 shows how this band edge straightening effect is quite significant for the wavelength range and materials considered here, and must be considered when comparing to the experimental results of Section 4.2.

Variations in the filling liquid refractive indices should also be taken into account. According to the specifications of the supplier (Cargille^{TM}), the natural material dispersion of the liquids is negligible (orders of magnitude lower) in comparison with the dispersion of the layer materials. The dominant influence on the liquid refractive indices is thus likely to come from the effects of temperature variations. Throughout the experiments, no temporal dependence was observed in the transmission spectra, indicating that local heating of the liquids due to the light source is negligible; unsurprising since the liquids are transparent in, at least, the visible spectrum. Thus, it is assumed that temperature variations predominantly arise from atmospheric variations. Given the sensitivity of refractive index over temperature given by the official data sheets for the liquids, the

variation of the liquid indices is approximated here to be ±1%. The horizontal dashed and solid lines in Fig. 4.5 represent the upper and lower limits, respectively, of this approximated variation in n_{core}.

In order to compare the Bloch-wave bandgap maps (Fig. 4.4) with the observed experimental transmission spectra, the band edges between which a given mode resides must be determined. This is relatively simple for the given regime since one can assume the lowest-loss guided modes all lie very close to the n_{core}-light-line, as discussed in Chapters A.4 and 2.4. Given this, it is fair to assume the guided modes will lie between the points where the n_{core}-light-line itself intercepts the bandgap edges. Figure 4.5 represents this for the considered fibre and liquids: Each liquid refractive index corresponds to a particular horizontal line; The intercepts of these lines with the bounding TM bandgap edges are represented by the associated vertical lines dropped to the horizontal axis. To accommodate for the aforementioned potential ±1% variation in n_{core}, since the gap edges are generally monotonically decreasing with λ, the short-λ edge is taken as the intersection of the upper n_{core} limit (dotted horizontal line) with the TM gap edge and the long-λ edge as the intersection with the lower n_{core} limit (solid horizontal line). The transmission spectrum of a fibre with core index n_{core} and cladding structure producing such bandgaps would thus be expected to transmit light predominantly in the wavelength region between the band edges bound by the pair of vertical lines corresponding to the appropriate value of n_{core}.

Figure 4.5 demonstrates how the experimentally measured transmission spectra do indeed align with the aforementioned theoretically predicted bandgap edges for all considered values of n_{core}, but only when the layer material dispersion (Fig. 4.3) is considered. This agreement can be appreciated moreso when one compares it to the bandgap edges calculated when material dispersion is neglected (Fig. 4.5 bottom). When material dispersion is 'turned off', in this case by arbitrarily setting $n_{\text{As}_2\text{S}_3,\text{PEI}}(\lambda) = n_{\text{As}_2\text{S}_3,\text{PEI}}(700\text{ nm})$, all calculated bandgaps are shifted to lower values of λ. While the transmission peak for $n_{\text{core}} = 1$ still sits within the predicted band edges, the edges are widened and pushed toward shorter λ somewhat such that the transmission peak lies closer to the longer λ region band edge, rather than close to the midpoint of the edges. More strikingly, this effect is more severe for the other peaks (corresponding to $n_{\text{core}} = 1.4019, 1.4620$, and 1.5780) where, once material dispersion is neglected, the gap edges barely align with their associated transmission peaks at all. Indeed, the calculated short-λ edge of the gap corresponding to $n_{\text{core}} = 1.5780$ (blue lines in Fig. 4.5) resides beyond the displayed axis limits, excluding the experimentally measured transmission peak from the bandgap region all together. From this one concludes that the incorporation of the layers' material dispersion is vital in order to predict the position of the

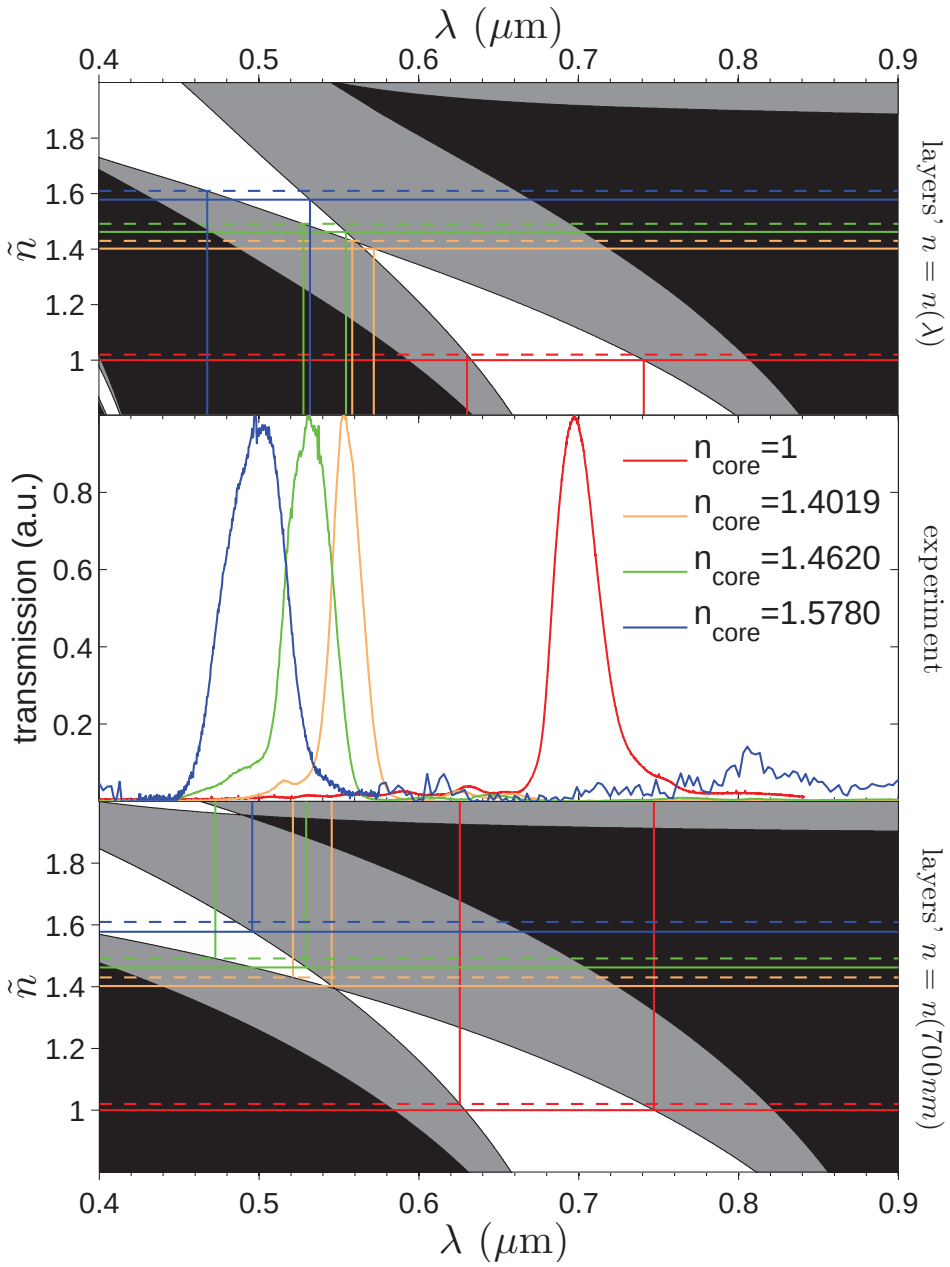

FIGURE 4.5: The experimentally measured transmission spectra from the Bragg fibre filling setup (Fig. 4.1) using liquids of various refractive indices (as well as the empty case). The associated bandgap spectra including and ignoring layer material dispersion are aligned above and below (respectively) the measured transmission spectra'.

bandgap edges, as might be expected from the large variations of $n_{As_2S_3}$ and n_{PEI} as $\lambda \to 0$ alone (Fig. 4.3).

Only the TM bandgap edges have been considered in the above analysis because they represent the dominant bandgap for randomly polarised light, which is in agreement with the observations of [42]. Both TM_{0n} and HE_{mn} modes contain TM field components and hence succumb to the effects of the TM bandgap. Since no effort is made to excite a particular mode class (*e.g.*, only the TE_{0n} modes), one can assume most modes excited

in the fibre contain TM ray components which, when residing within a TM band, will be preferentially coupled out through the cladding due to the Brewster-type transmission effect (the effect that makes the TM gaps smaller than the TE gaps, Chapter 1), *i.e.*, the TM bandgap edges will predominantly define the low-loss region of such a waveguide when most excited modes contain TM field components.

The TE gap still plays a significant role in the confinement process, especially in the regions close to the Brewster condition (where the TM gap closes up, Chapter 1). Within the TE gaps, once the TM ray components have been filtered out due to the increasing dominance of the Brewster effect, the TE components are left behind. This explains the existence of an obvious transmission spectrum for light propagating close to the TM gap closure point (the Brewster condition), such as exhibited by the $n_{\mathrm{core}} = 1.4019$ case in Fig. 4.5. A more convincing analysis of this behaviour would require both more transmission spectra to be measured for filling liquids with refractive indices about the Brewster point n_{B} and a more thorough theoretical description of the propagation mechanism, possibly via either an eigenmode treatment or, more appropriately for the large-core regime considered here, a vectorial beam propagation simulation.

4.4 Concluding Remarks

The shifting of a Bragg fibre's transmission spectrum by filling the core with liquids of various refractive indices has been experimentally demonstrated. At the time of presentation (at the Conference on Lasers and Electro-Optics 2009 [55]) these results represented the first demonstration of transmission band shifting via scaling solely the core refractive index in a solid-cladding HC-MOF (and, to the best of my knowledge, still the only demonstration).

Reasonable agreement with what is expected from a Bloch-wave based analysis was achieved, but only when the material dispersion of the layers was incorporated (something typically not incorporated into bandgap calculations). The layers' material dispersion acted in such a way that the band edges became more linear over the frequency spectrum, rather than their characteristic asymptote-like trend towards the low-index light-line. This material-induced band edge straightening was verified in both experiment (by the approximate linearity of the peak shifting with core index, *e.g.*, § 4.2) and theory (by calculation of the bandgap maps incorporating the experimentally derived material dispersion, *e.g.*, § 4.3).

These results verify some of the key features of variable core refractive index (including liquid-filled) low-index guiding multilayer waveguides discussed in Chapter 3, pointing a

way towards the application of liquid-core Bragg waveguides (and hence also I-ARROW waveguides, as per their equivalence argued in Chapter 3 and its partner publication, Ref. [61]) in sensing, microfluidics, fibre lasers, and novel nonlinear devices [19]. Owing to the similar, multilayer cladding, geometry, these results can also be applied to investigations of the design and operation of SEFLs [30] with cores of varying refractive index. As an explicit example, the fibre used in this work demonstrated a transmission peak sensitivity to core refractive index of $\partial\lambda_0/\partial n_{\text{core}} \approx 330$ nm/RIU, which is comparable with the results of a similar I-ARROW based architecture (which relies on detection of a transmission minimum, not maximum as used here) [59].

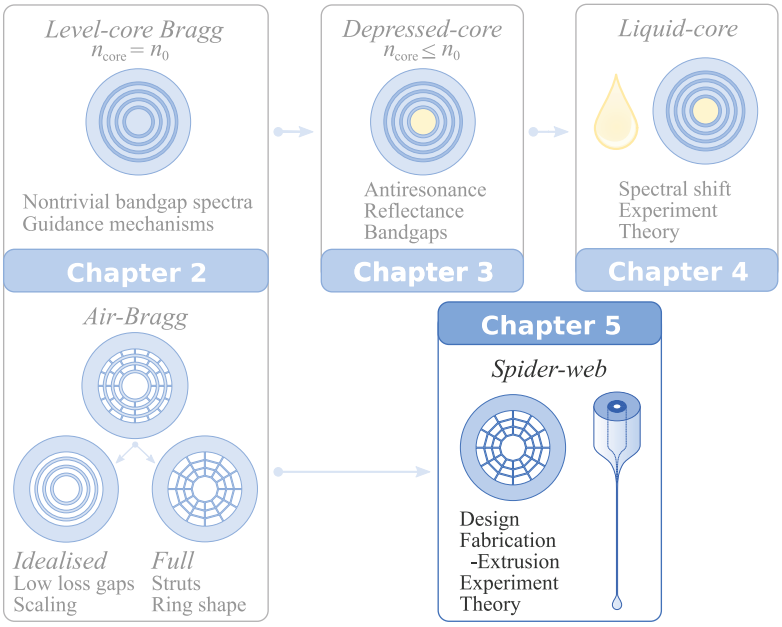
Level-core Bragg
$n_{core} = n_0$
Nontrivial bandgap spectra
Guidance mechanisms
Chapter 2
Depressed-core
$n_{core} \leq n_0$
Antiresonance
Reflectance
Bandgaps
Chapter 3
Liquid-core
Spectral shift
Experiment
Theory
Chapter 4
Air-Bragg
Idealised
Low loss gaps
Scaling
Full
Struts
Ring shape
Chapter 5
Spider-web
Design
Fabrication
-Extrusion
Experiment
Theory

Chapter 5

Soft-Glass Air-Bragg Fibres via Extrusion

THE initial principal goal of my research toward this thesis was *the fabrication of a demonstrably guiding soft-glass photonic bandgap fibre via the extrusion method*. In what follows, I will demonstrate the modest success that has been born from this work.

There are a few approaches to this goal. Discussed by way of introduction will be: the motivation and the most promising approaches; explanation of the choice of an effectively 1D-cladding fibre structure (an air-Bragg fibre design); and how the extrusion preform fabrication technique ideally compliments the process, especially for soft-glass substrates. The successes of this work thus far, both in terms of fabrication progress and observed guidance properties will then be discussed, concluding with a comparison of the experimental results with numerical modeling.

This chapter is a considerable extension upon the work reported at the conference proceedings of the Australian Conference on Optical Fibre Technology (ACOFT), 2009, oral presentation (K. J. Rowland) [175]—authors: K. J. Rowland, H. Ebendorff-Heidepriem, S. Afshar V. and T. M. Monro. The presentation was awarded the Wanda Henry Prize for 'best student presentation'.

5.1 Motivation and Fabrication Method

The motivation for the fabrication of soft-glass air-guiding fibres is relatively simple. As discussed at length in Chapter 1, silica hollow-core microstructured optical fibres are a proven and well-understood air-guiding platform, both theoretically and experimentally. As discussed, this is primarily due to the very well-understood properties of silica glass, having been used in optical fibre fabrication for many decades. However, the use of

silica glass restricts the cross-sectional structures and refractive indices from which a HC-MOF can be made: capillary stacking is capable of producing only a limited range of cross-sectional fibre structures and silica itself has a refractive index $n_{Si} \approx 1.45$ (up to material dispersion: $\approx \pm 0.01$ over the visible to near-infrared spectrum), *e.g.*, capillary stacking has been used for the fabrication of hexagonal-, honeycomb-, Kagomé-, and square-lattice silica HC-MOFs (as discussed in § 1.2).

The most appealing benefits of non-silica substrates, such as soft-glasses, are at least three-fold. Depending on the glass composition, soft glasses have potential benefits for HC-MOFs owing to their:

- larger range of refractive indices,
- lower transformation temperatures, hence a greater variety of fabrication techniques,
- greater variety of low material-loss transmission windows.

The range of refractive indices from various soft-glasses are from about 1.5 (e.g. boro- and lead-silicate glasses [89, 90, 205]) to 3.3 (chalcogenide glasses [84–88, 206, 207]) and a continuum in between (accessed by appropriately altering the amount of various chemical compounds used in the 'recipe' of a given glass). As discussed in § 1.2.3, larger substrate refractive indices can produce guidance regimes in which core modes of hexagonal-lattice HC-MOFs can access high-order bandgaps which don't exist for lower refractive index substrates like silica—numerically analysed in Ref. [76, 82, 83].

Another way of accessing a wider range of guidance regimes is to alter the geometrical structure of the waveguide. Owing to the high transformation temperatures of silica glass, the stacking of thin-walled capillaries has proven to be the most effective fabrication method for HC-MOFs. The various geometries attainable using this technique were discussed in detail in Chapter 1. The capillary-stacking method is now standard for the fabrication of air-guiding silica HC-MOFs [2, 3, 81, 126], and is a straight-forward extension of a similar technique used for solid-core PCFs [2, 3]. In both cases, silica capillaries are precisely stacked in a hexagonal/trigonal lattice within a 'jacket' tube which hold them all together (also made of silica). To make a hollow core, several capillaries are removed from the centre of the structure, leaving a defect in the lattice. The trigonal pattern represents the optimal packing possible for such capillaries in 2 dimensions and so is the most common geometry for the fabrication of silica HC-MOFs, although there are a few variations as mentioned above (such as the Kagomé- and square-lattice variants). This packed structure forms the fibre *preform*.

Capillary-stacking can also be applied to soft-glass microstructured fibre preforms. Recent examples of successful stack-and-draw processes for soft-glass (solid-core) MOF

fabrication have been demonstrated by Refs. [85, 86, 88, 94, 208]. However, since such glasses have significantly varied properties depending on their composition, much development is required to produce capillaries of the required optical quality and uniformity, unlike the ubiquitous silica glass; the development of refined capillary fabrication techniques is required. Furthermore, true to their name, soft-glasses are much more easily scratched and fractured than silica, making it difficult to produce preforms in which the interfaces between all capillaries are ideal; a small scratch or crack in a capillary could manifest as a significant defect in the final fibre cross-section.

Even with silica's benefits, its high softening temperature ($\approx 1700°C$) has seen that the fabrication of silica MOFs is restricted solely to the capillary-stacking technique; the methods and materials used in other preform fabrication techniques have not yet shown to be suitable at such high temperatures. Soft-glasses, however, have much lower transition temperatures than the conventional silica glass, typically in the range of about $300°C - 600°C$ depending on the glass composition. It is the availability of lower fabrication temperature windows that makes these glasses amenable to other, more flexible, fabrication techniques. One such technique is *extrusion*: the principal preform fabrication method used in this work. The details of the extrusion of soft glass are presented in the next section.

Arguably, the final point above resembles the most important restriction of silica glass to circumvent: the finite low-loss transmission window of silica. The 'infra-red edge' of silica (the wavelength beyond which the glass most absorbs long-wavelength light) exists at a wavelength of about 2.5 μm [178]; light of longer wavelengths is heavily attenuated, making silica essentially opaque above the infra-red edge. The IR edge is due to vibrational modes of the silica lattice, which are centered between 7 μm and 11 μm, with anharmonic coupling broadening the absorption down to the NIR [178]. There is an ultra-violet (UV) edge below which light is strongly attenuated; this absorption is predominantly due to the electronic bandgap of the material in the visible spectrum, but becomes dominated by Rayleigh scattering within the NIR spectrum [178]. The low-loss guidance of light in the Near- to Mid-IR spectral regions is a very promising area for applications in areas such as medicine, high-power delivery, sensing and nonlinear optics. High-power delivery using a hollow-core Bragg fibre has been demonstrated [11, 41, 42], but as discussed in Chapter 1 the fabrication technique for these HC-MOFs is not easily scalable down to small core sizes, as desirable for applications beyond high-power delivery in which control over the modal dispersion and an enhanced peak intensity is desired. The alternative to the solid multilayer cladding Bragg fibre geometry is the fabrication of a single-material HC-MOF capable of low-loss guidance in the infra-red spectrum. Even though the field overlap of the guided light with the cladding structure is very small in most state-of-the-art silica HC-MOFs ($\sim 1\% - 5\%$, [18, 140]), it is still

large enough for the material loss to become the dominant loss mechanism beyond the IR absorption edge. For example, assuming 1% of the guided light intensity overlaps with the substrate material but a large material loss of 10 dB/km, say (as would have silica in the MIR spectrum), the power loss of the guided mode would be of the order of 100 dB/m; this level of loss to the material itself (not incorporating confinement loss here) would enforce a limit to the amount of power able to be guided before the substrate itself is damaged.

The use of soft-glasses has the potential to extend the transmission window of HC-MOFs into the NIR to MIR. Soft glasses have the potential to circumvent this absorption, in particular chalcogenide glasses which can exhibit low material absorption well into the MIR spectrum [84–88, 206, 207]. There are many other soft-glass compositions which hold similar interest. The types considered here are bismuth oxide and lead silicate glasses (discussed further later) that, while they don't have transmission windows that extend well into the MIR, have optical and fabrication properties that are enough for proofs of principle and interest in their own right.

All of these degrees of freedom are fundamental to accessing the potential landscape of guidance properties available from air-guiding fibres. By designing HC-MOFs with various substrate refractive indices and low-loss transmission windows using unconventional cross-sectional geometries, regimes of unprecedented bandwidth, modal loss, dispersion, etc., will become accessible. The use of soft-glasses has the potential to access such points in this landscape of guidance regimes and fibre designs. Of most interest for this work is the possibility to use a novel method in the fibre preform fabrication process: extrusion—ideally suited to soft-glasses.

Given the flexibility offered by the extrusion technique, I decided a promising fibre geometry to fabricate would be a variant of the air-Bragg fibre discussed in Chapters 1 and 2; namely, a Bragg fibre whose cladding consists of alternating concentric rings of glass and air. The rings must be supported by connective struts in order to represent a realistic, fabricable, fibre structure. The air-Bragg fibre structure is appealing in that it has already been demonstrated in silica as supporting very wide low-loss transmission regions [43] in a geometry almost representing the ideal structure of solid concentric rings suspended in air, as discussed in Chapter 1. The final fibre design also exhibits many of the structural principles of the Kagomé- and square-lattice type fibre structures (Chapter 1) in that it represents concentric polygons supported by connective struts and hence predominantly exhibits an antiresonance type guidance mechanism; there are particular parallels here to the numerical modelling results of Ref. [145].

The following sections detail the design principles employed and the success and failures encountered in implementing them. Of particular note is the way in which the

produced structures exhibit properties that would be very difficult, if not prohibitive, under conventional fabrication techniques such as capillary stacking. One such example is the fabrication of colinear struts supporting rings of constant pitch (§ 1.4), as will be demonstrated.

It should be noted that there are other preform fabrication techniques such as *casting* and *drilling*. Casting involves pouring the glass in molten form onto a die structure, rather than slowly pushing softened (not molten) glass thorough a die; when solidified[1], the glass can then be lifted from the die structure to reveal the cast preform. An impressive example of casting a soft-glass (chalcogenide) structured preform was reported by Coulombier et al. [91]. Drilling is at it sounds: drilling holes directly into a solid billet of glass using a precision drill press. Drilling is routinely employed in the fabrication of structured polymer preforms, such as in Ref. [66]. Drilling can even be employed for silica MOF fabrication, and was actually part of the process used to fabricate the first demonstrated MOF by Knight et al. [209], but in terms of internal surface quality (discussed further presently), the process is inferior to the refined stacking technique used for silica MOFs today [2, 3].

Casting and drilling limits the length of the preform to the length of the die features or length of the drill bits (the latter of which, incidentally, can only produce circular holes of a minimum diameter for mechanical reasons). The extrusion method on the other hand can produce almost arbitrarily long preforms owing to the fact that the softened glass is continuously pushed through the die; the extruded parts of the continuous preform solidify once sufficiently far from the die exit face. Also, methods such as the casting and drilling fabrication methods are often unsatisfactory in terms of surface quality and glass temperature cycle effects such as crystallisation [90]. These adverse effects degrade the inner and surface structure of the glass itself, inducing scattering or absorption centres in the resultant waveguide; although there has recently been some very promising success with the casting of microstructured chalcogenide preforms producing very low-loss fibres [91].

These potential negative effects are circumvented somewhat with the extrusion method, owing to the fact that extrusion is a relatively less severe process in both glass transformation time and temperature ranges and rates [90]. While this is part of the reason for employing it here, another reason is more to do with circumstance in that extrusion is also the technique with which the research group I have been part of while conducting this research is most familiar and for which the available fabrication facilities were best equipped to provide. Fabrication quality and circumstance aside, the most appealing

[1]Glass is an amorphous solid with identifiable phase transitions, not simply an extremely viscous liquid as often claimed by the lay-person [90].

aspect of the extrusion technique here is its potential to produce almost arbitrary cross-sectional structures—vital for the creation of the spider-web fibre structures that will be demonstrated below.

5.2 Soft-Glass HC-MOF Fabrication via Extrusion

The fibre fabrication process used for this research is now described, with special attention given to details of the soft-glass extrusion process. Section 5.2.1 details the extrusion technique used to fabricate the structured soft-glass preforms. Section 5.2.2 then discussed the fibre drawing technique used to fabricate fibres from these preforms.

5.2.1 The Extrusion Technique

The extrusion technique as used in this work is a method of making a fibre *preform*: the macroscopic precursor to a fibre itself. The extrusion technique involves the transformation a solid billet of glass (e.g. Fig. 5.1, left) into a structured preform [90]. Figure 5.2 shows a schematic representation of the process. This is achieved by increasing the temperature of the glass to a point where it softens sufficiently (typically about $300°C - 600°C$ for soft-glasses, depending on the glass composition [90]), at which point it can be pushed through a solid *die*. As described above, the extrusion die is a typically metallic structure (stainless-steel here) whose exit-face exhibits the inverse cross-sectional structure desired for the fibre preform. An example of an extrusion die as used here is shown in Fig. 5.1 (right).

FIGURE 5.1: *Left*: a 5 cm diameter soft-glass (lead-silicate, F2) billet. *Right*: the exit-face of a spider-web structure stainless-steel extrusion die used for soft-glass preform fabrication (same as in Fig. 5.8). Like this die, all dies made to extrude glass billets of diameter 5 cm shown here have a exit-face outer rim diameter of about 44 mm and entrance diameter of about 5 cm.

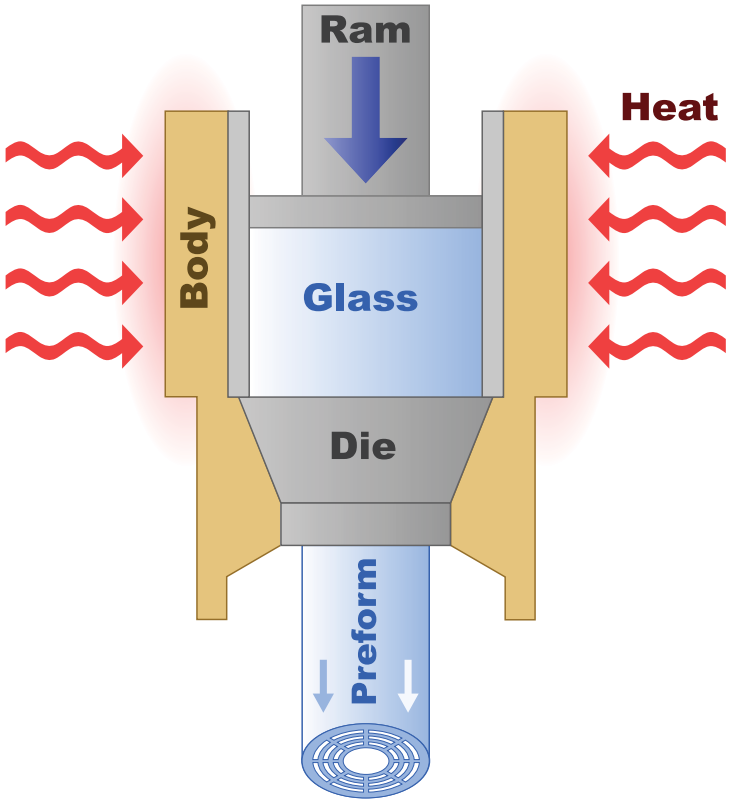

FIGURE 5.2: A schematic of preform fabrication via extrusion. Details in the text.

The apparatus used to achieve this extrusion typically consists of a metal body which holds the die and glass billet which, once heated, is pushed through the structured die via a mechanised ram. These components are placed within a furnace and heated to the precise target temperature at which the glass softens sufficiently. A schematic of the extrusion apparatus is shown in Fig. 5.2. In more detail, a billet of glass is placed on top of the structured extrusion die, both held within a thick-walled stainless-steel body. The glass is shielded from the body's inner surface by a cylindrical stainless steel sleeve. A circular plate is placed on top of the glass billet, upon which the mechanised ram pushes. The whole structure is placed within a furnace and heated to the temperature at which the glass softens sufficiently to be pushed through the vacant channels of the die by the ram. The structured glass preform is formed once the glass passes the die's exit face and cools. All of the components with which the glass comes into contact are cleaned thoroughly using an ultrasonic cleaning bath with de-ionised water and detergent—the components are subsequently rinsed with distilled water, then methanol, before assembly for the extrusion process, ensuring the glass is not contaminated with impurities or even water[2].

[2]Water content within the glass or on its surface can produce significant defects within the final preform due to the production of water vapour upon the heating of the glass within the presence of water, say. This can result in bubbles within or on the surface of the preform.

In order to produce satisfactory extruded preforms, the precise values of ram speed (hence pressure on the glass and die) and furnace temperature (hence viscosity of the softened glass) require both quantitative knowledge of the glass properties, including its flow dynamics, but also qualitative practical experience with the extrusion technique in general. If the extrusion parameters are not employed correctly, the extrusion process can produce less than desirable results due to excess deformations in the extruded glass structure due to undesirable flow dynamics or (more severely) due to the die itself deforming or breaking under excess pressure.

Since all fabricable microstructured fibres must have simply-connected glass regions in their cross-section (all regions must have structural support), an extrusion die cross-section often appears as a collection of solid 'islands' (Fig. 5.1, right). The islands block the flow of glass, leaving corresponding holes in the preform. One will notice how these solid features of such a die appear disconnected from each other. This mechanical problem is overcome by anchoring these solid islands to a common plate containing an array of small holes (obfuscated in most images of dies here, but visible in Fig. 5.13, left), named a 'sieve-plate' owing to its appearance, not its behaviour (all incident glass on the sieve plate passes through the holes in the plate). These holes allow the glass to flow through into the primary structured region of the die while holding the die structure together [90].

So, provided the glass regions in the design's cross-section are simply-connected, almost *any* preform structure can be extruded, up to the limitations on die fabrication and glass fluid-dynamics. In this way it is apparent how the extrusion technique offers an effectively infinitely greater variety of preform structures to be created than by using the restrictive capillary-stacking technique. Extrusion is restricted to soft-glasses because their lower softening temperatures permit the use of machinable materials, like stainless steel, for complex dies; no such materials exist for the working temperatures required for silica glass. The examples demonstrated presently show structures that are inaccessible to conventional silica fibre fabrication, and represent some of the possibilities presently at the forefront of glass extrusion today.

5.2.2 The Fibre Drawing Process

No matter the preform fabrication process, once the preform is made it is then reduced to smaller dimensions via the *fibre drawing* process; the result is the desired optical fibre. The reduction of the preform down to fibre dimensions is termed *fibre drawing*. A schematic of the process is shown in Fig. 5.3.

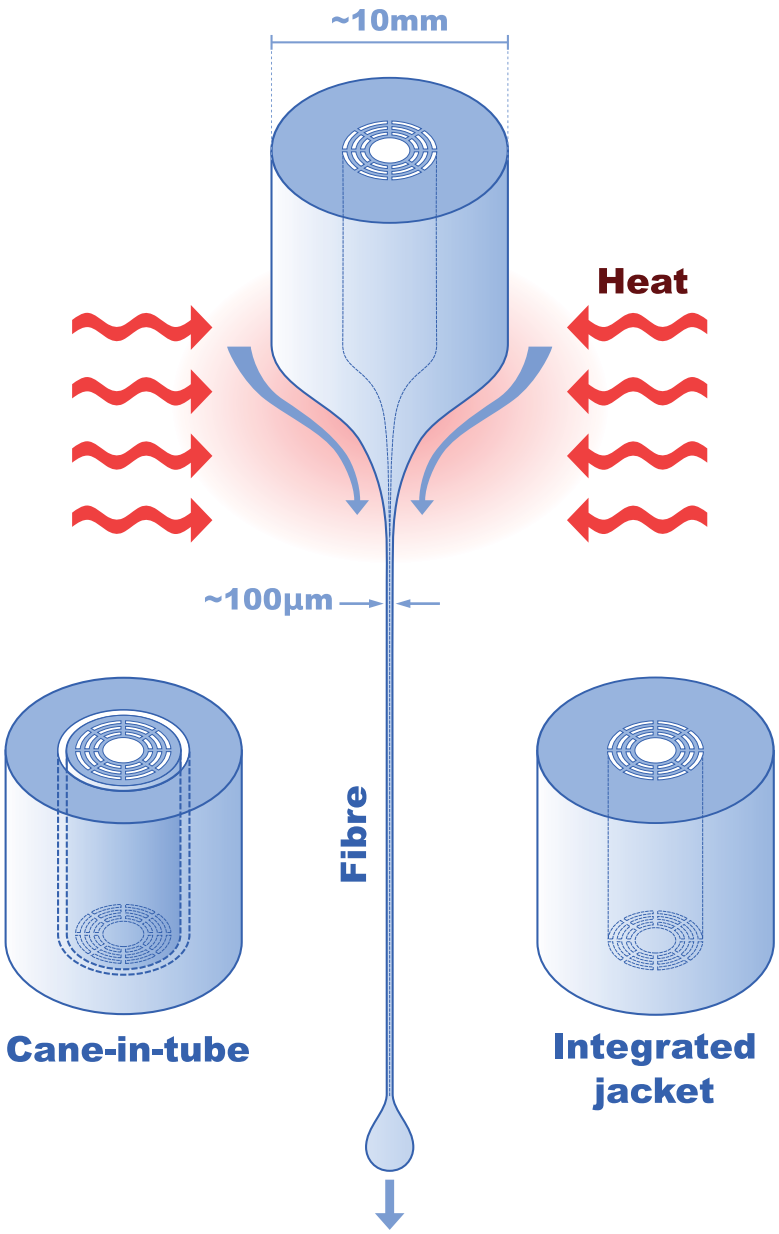

FIGURE 5.3: *Centre:* A schematic of fibre drawing from preform. *Left:* A preform constructed via the cane-in-tube concept; permits structured regions far smaller than those fabricable directly from extrusion. *Right:* A full preform made directly from extrusion utilising an integrated jacket, avoiding the need for structural support via the cane-in-tube technique but limited to the smallest structural feature sizes permitted by the die. Details in the text.

Drawing the preform to fibre involves holding the preform vertically in a fibre drawing *tower*. A schematic representation of the process is shown in Fig. 5.3. The bottom end of the preform is heated to a temperature about $50°C - 100°C$ higher than required for extrusion ($\approx 700° - 800°$ for the soft glasses used here). At this temperature, the glass begins to become more liquid or 'runny'. When this temperature range is reached, a drop of glass will form at the base of the preform due to gravity and surface tension

effects. Much like honey dripping from a spoon, this drop then falls away from the preform, leaving behind it a connecting strand of glass. If the temperature of the preform and internal pressure of the holes is tuned correctly, the structure will be preserved throughout the length of this connecting strand, as depicted in Fig. 5.3 (centre). With these conditions maintained, the glass will continue to flow in this manner, drawing down the preform structure into a thin fibre of outer diameter $\approx 100\ \mu m - 250\ \mu$m. As it is pulled from the preform, the fibre is continuously wound around a drum, allowing the fibre to be pulled from the preform until as much of the preform material as possible is consumed.

Often when smaller structural features are desired but within practical fibre outer-diameters ($\approx 100\ \mu m - 250\ \mu$m), the preform is first drawn down to a *cane*: an intermediate structure somewhere between a preform and a fibre. The outer-diameter of a cane is typically a few mm in diameter, rather than $\sim 100\ \mu$m as for the fibre. The cane drawing process is similar to fibre drawing except that the cane must be kept straight during the draw owing to its larger structure compared to the fibre; the glass only becomes flexible enough to wind onto a drum once the fibre diameter reaches $\lesssim 250\ \mu$m or so, depending on the glass composition. The cane is then inserted into a thick-walled *jacket*; a tube of the same glass typically with similar macroscopic dimensions to the initial preform, as depicted in Fig. 5.3 (left). The jacket tube is also fabricated by the extrusion process. This is often imaginatively referred to as the *cane-in-tube* technique. The composite preform (cane inside the tube jacket) is then pulled down to fibre in the same way as the direct preform-to-fibre method just described.

By introducing an intermediate drawing step (caning) and then adding extra material (the jacket) to the outside of the structure, the preform structure can be pulled down to far smaller dimensions than possible with direct-drawing. Note that the relative size of the cane to the outer diameter of the jacket can be varied considerably and is not restricted to the relative sizes depicted in Fig. 5.3. Attempting to produce, via direct-drawing, features on the small scale achievable via the cane-in-tube method, would produce a an unmanageably fragile fibre due to the very small outer-diameter required (tens of microns, say)[3] in the absence of a buffering jacket.

Also, by using a cane-in-tube method, the full real-estate of the die can be exploited to embed more structure into the preform cane than would be possible on a preform with an integrated jacket since the solid jacket region required for structural integrity for the latter takes up space on the die. It is very important to note that, in order for the small

[3]There is a range of outer-diameters within which a glass fibre is sufficiently 'bendable' and generally manageable owing to a combination of the mechanical and thermal stress properties of the particular drawn glass and the structure fabricated into it. Certain glasses may be more or less fragile based on their chemical composition, but a significant proportion of air within a cross-sectional structure typically increases the fragility regardless of the glass type.

gap between the cane and tube to be closed during drawing, a vacuum must be created over the interface. This vacuum must not be applied to the cane structure, or else the holes would quickly collapse.

This is related to a very important observation. Pressurisation of the holes within the structure during the fibre drawing process is critical in determining the ultimate cross-section of the microstructured fibre. In the absence of adequate internal hole pressure, the structure of the preform would collapse upon heating, producing a simple stand of glass without any internal structure. There are two ways to pressurise a structured preform during the fibre drawing process: *self*-pressurisation or *active*-pressurisation.

Self-pressurisation is just as its name suggests: the exposed (non-drawn) end of the preform is sealed off (by blocking the holes of a preform or melting the end of a cane, say), allowing the pressure of the holes themselves to build up as material is pulled from the preform during the drawing process. One side effect of this is that the pressure within the holes increases as the draw goes on, owing to the fact that preform material is being removed while both ends of the preform are effectively sealed (the holes of the fibre being small enough to restrict significant air flow though them). The dynamics of this self-pressurisation fibre drawing process are significantly nontrivial, meaning that refinement of the microstructured fibre drawing process has historically been a matter of empiricism, intuition and practical knowledge. There has recently (mid-2009) been some impressive theoretical analysis on the dynamics of drawing microstructured optical fibres by Voyce et al. [177] in which an analytic treatment was employed, requiring almost 30 physical parameters to describe the preform, air, and furnace properties; the final problem becomes a complex interaction of thermal, mechanical and fluid dynamics. While the model was elegant and robust, it was still only for the simple case of a tube or capillary (a single circular hole), highlighting the fact that the analysis of more complicated structures is an incredibly complicated problem requiring the interactions of many physical concepts. Of most importance, though, is that it demonstrates how and why the self-pressurisation method works and why it works so well.

The results of Ref. [177] also demonstrate how easily instabilities in the fibre drawing process can occur, manifesting themselves in fluctuations in the scale of the fibre cross-sectional structure, for example. In practice, under the drawing conditions used for the fibres fabricated for this work, one can reduce these fluctuations to about $\pm 1\ \mu\text{m} - 2\ \mu\text{m}$ of the fibre's outer-diameter. This is a very important point and is a critical consideration for later analysis.

Active-pressurisation, alternatively, involves sealing the exposed end of the preform to a controlled gas source, allowing arbitrary pressurisation of the holes. Active pressurisation may provide another degree of freedom during fibre drawing, but it is an inherently

sensitive procedure; the internal pressure of the preform/fibre must stabilise before the effects of pressure changes can be determined and with only a finite amount of material to draw, this requires both experience and skill to perfect owing to the fact that the parameter window required for stable drawing is very small: if the pressure is too small, the structure typically collapses on itself; too large and one risks damaging the structure due to over-inflation (often resulting in the draw-down region ballooning out, similar to the way a professional glass-blower inflates their samples). Further, soft-glass is inherently fragile, making active-pressurisation even more challenging as the fibre strand can fracture under the stress induced by inflation, depending on the drawing parameter regime.

The downside of the cane-in-tube technique is that, due to the geometry of the composite structure (a cane completely surrounded by a jacket-cane interface), one can only pressurise the cane *or* apply a vacuum to the interface at one time. To achieve both an interface vacuum and cane pressure requires a setup in which the tube supplying the pressure to the cane passes through the wall of the vacuum seal over the interface; while this can be done, it is typically a very nontrivial setup to achieve. Given this, cane-in-tube drawing is often done only with self-pressurisation of the cane (by melting the exposed end). The ramifications of this on the fibre fabrication results here are discussed in the following sections.

The next section details the results I have so far achieved in the pursuit of fabricating an extruded soft-Glass air-Bragg fibre, both failures (from which the technique is refined) and successes. Given the success I report presently, the fabrication technique will open up the possibility of fabricating other similar structures via extrusion, such as hollow-core fibres with a Kagomé-lattice, or air-Bragg fibres based on other concentric cladding shapes such as squares rather than rings; possibilities that are inconceivable by any other fabrication technique. Further, the extrusion technique makes this possible using a variety of substrates [90], from polymers to soft-glasses to any other optical material capable of being extruded to sufficient quality.

5.3 Fabrication Results

Due to its complexity, fibre fabrication is often an iterative process, requiring the fabrication of many intermediate attempts in order to determine the appropriate fabrication regimes for the case at hand. The soft-glass air-Bragg fibre fabrication here is no exception. The results that follow demonstrate how the results of fabrication trials—the properties of the structured glass itself—can be a determining guiding factor in the design process. As mentioned earlier, microstructured fibre fabrication is an incredibly

Preform	Fibre	Die/Fibre Structure	Glass
1	–	Offset, $t_{\text{ring}} > t_{\text{strut}}$, 4-ring, cane-in-tube	Bi-oxide
2	A	Offset, $t_{\text{ring}} = t_{\text{strut}}$, 4-ring, cane-in-tube	Bi-oxide
2	B	Offset, $t_{\text{ring}} = t_{\text{strut}}$, 4-ring, cane-in-tube	Bi-oxide
3	C	Colinear, $t_{\text{ring}} = t_{\text{strut}}$, 4-ring, cane-in-tube	Lead-silicate
3	D	Colinear, $t_{\text{ring}} = t_{\text{strut}}$, 4-ring, cane-in-tube	Lead-silicate
4	E	Colinear, $t_{\text{ring}} = t_{\text{strut}}$, 2-ring, integrated jacket	Lead-silicate

TABLE 5.1: Summary of air-Bragg preform extrusion and fibre fabrication.

complicated physical system, making predictions of the fabrication behaviour of a given glass and structure incredibly difficult. Nonetheless, some guiding principles can be determined from which can form part of the basis for iterative refinement in combination with design requirement from simulation and knowledge of the light guidance properties required from the waveguide. The results I present are quite promising, indicating that extrusion is a viable alternative means of HC-MOF fabrication, allowing one to design and fabricate fibres beyond the limits of conventional materials and techniques such as silica capillary stacking towards almost arbitrary structures in a plethora of extrudable optical substrate materials.

Table 5.1 contains a summary of all extrusion and fibre drawing results to be discussed, with information about the die structure, glass composition, and brief comments on the results. Each preform and fibre fabrication result is discussed sequentially as it appears in the table (top to bottom).

5.3.1 Offset Struts

The first attempts at preform extrusion for the air-Bragg fibre used a bismuth-oxide glass, orange in appearance since the bulk transmission window lies closer to the NIR spectrum, opaque to most of the short-wavelength visible light. This glass has a refractive index of about $n_{\text{Bi}} = 2.0$ and a softening temperature of approximately $480°C - 490°C$. This particular glass was supplied by Asahi Glass, Japan. The particular die used, Fig. 5.4 (left), was based on a similar die used previously to extrude a polymer preform (which was not developed further); the polymer preform in question can be seen in [90]. The use of this die was primarily proof-of-principle, demonstrating that the extrusion of such structures is possible with soft-glass. Particularly noteworthy is that the die was designed with *offset* struts; the struts connecting adjacent layers were placed so as to minimise the chance of being colinear with one another (the air layers containing either 6, 9, 12, and 16 struts). This principle simply followed from the design of the silica

FIGURE 5.4: **Preform 1**. *Left*: Photograph of the exit-face of the stainless-steel die used to extrude a 5 cm diameter bismuth-oxide glass billet to create the initial air-Bragg fibre preform. *Right*: Photograph of the end of the produced preform (a glass-cutting saw has been used to produce a clean, flat, end-face). The diameter of this section of the preform is about 2 cm.

air-Bragg fibre of Vienne et al. [43], under the impression that, in the final fibre, tunnelling of the light through the cladding would be minimised. As was discussed in § 2.7, the placement of the struts with respect to each other doesn't have a great effect on the guidance properties (at least as far as the general CL spectrum structure is concerned); this gives more freedom to the placement of the struts between rings during the design process. Also, the struts in this case are designed to be thinner than the concentric rings ($t_{\text{ring}} > t_{\text{strut}}$), also in line with the design of the fibre of Ref. [43]. However, a thorough study is required to reveal the effects of the presence of struts (extending on the work of Ref. [70–72] and the new results presented in § 2.7) over the behaviour of the idealised structure, such as whether the thickness and placement of the struts can be designed to reduce confinement loss while maintaining a practical, fabricable structure.

The preform fabricated from this die, Preform 1 (Table 5.1), is shown in Fig. 5.4 (right). All practical samples of extruded preform, this and all subsequent samples, were cut to approximately 18 cm long. Note how the structure of the die was reasonably well replicated by the extruded preform. There were, however, deformations to the structure of the rings due to the surface tension of the heated glass essentially rounding off the sharp edges the struts make with the rings. The surface tension also produces an unbalanced force at each strut-ring junction, 'pulling' the ring structure into distorted shapes. This effect is most evident when there are fewer struts connected to a ring (*e.g.*, the first two rings about the core in Fig. 5.4), allowing each strut to deform a larger section of a given ring. This distortion effect becomes particularly important when drawing to fibre due to the higher temperatures and lower glass viscosity at the drawing temperature compared to the extrusion temperature, as will be shown soon, but not for this particular preform.

FIGURE 5.5: **Preform 2**. *Left*: Photograph of the exit-face of the stainless-steel die used to extrude a 5 cm diameter bismuth-oxide glass billet to create the second air-Bragg fibre preform. *Right*: Photograph of the end of the produced preform (sawed flat). The diameter of this section of the preform is about 2 cm.

The second trial of preform fabrication used a die with an almost identical structure to that used for Preform 1, but with considerably thinner rings (Fig. 5.7, left). Thinner rings are generally desired in order to shift the centre of the fundamental resonance to practical wavelengths, as discussed in many of the works discussed in Chapter 1. For example, recall Eq. 2.4 under which the first-order antiresonance wavelength occurs for resonance order $m = 1/2$. Rearranging Eq. 2.4 for the layer thickness, one finds:

$$t_{\text{ring}} = \frac{\lambda_m m}{2} \left[n_{\text{ring}}^2 - 1 \right]^{-\frac{1}{2}} . \tag{5.1}$$

For a target guidance wavelength of 1.55 μm, say, and an F2 glass refractive index of $n_{\text{ring}} \approx 1.6$, the calculated target ring thickness for the fundamental antiresonance is calculated using Eq. 5.1 as $t_{\text{ring}} \approx 300$ nm. This ring dimension represents the target of most designs considered here. As it turns out, this was too fine to fabricate within the current fabrication technique (improved inflation techniques being required, § 5.3.2), but very interesting results were nonetheless observed, discussed § 5.4.

Note that, in this case, the rings and struts are designed to have the same thicknesses ($t_{\text{ring}} = t_{\text{strut}}$), purely because they represent the smallest manufacturable channel feature sizes (0.6 mm) for the dies used at the time. Exceeding this limit may not be feasible, anyway, since the restriction in glass flow may induce too much strain on the die, leading to structural deformations in the die itself (and possibly breakage). This die deformation effect was observed in at least a couple of fabrication trials and, in one extreme case, the solid core region on the die was actually broken from the die itself due to excess pressure, registered as above $60kN$ of force on the ram (due to the glass

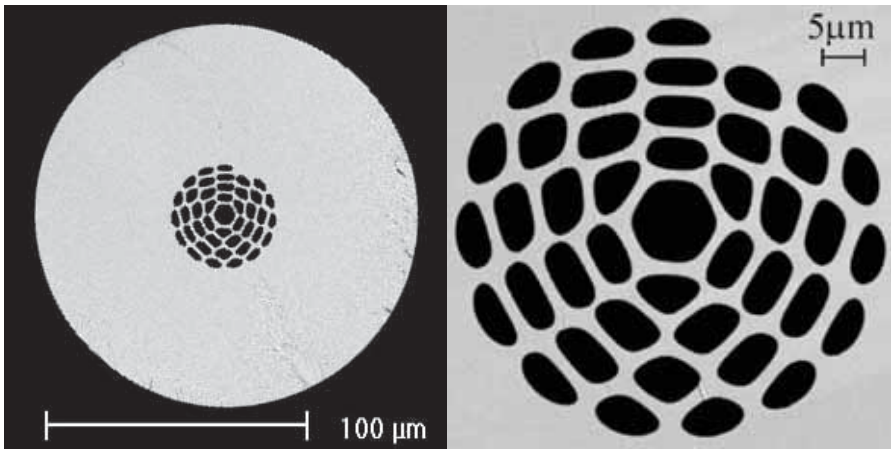

FIGURE 5.6: **Fibre A**. *Left*: A SEM of the first fabricated air-Bragg fibre using Bismuth Oxide glass. A cane-in tube technique was used after caning down a segment of Preform 2 (Fig. 5.8). *Right*: A magnified view of the structured region of the same fibre. One of the holes collapsed during drawing, leaving a solid region of glass in its place, distorting the structure further.

temperature being low—high viscosity—or the ram speed being too high—high force)[4]. The rest of the die designs shown here also use this $t_{\text{ring}} = t_{\text{strut}}$ design for the same reasons.

Preform 2 exhibits similar deformations as Preform 1, though less pronounced. This is likely due to the fact that the struts are now relatively larger than the those previously, making the surface tension effects less apparent. Nonetheless, the fact that the struts are offset from each other has remarkable implications when pulling this structure to fibre.

Fig. 5.6 shows a scanning electron micrograph (SEM) of a fibre pulled from Preform 2. The preform was first pulled down to a cane and then inserted into a hollow tube extruded from the same bismuth glass (explaining the much larger region of glass about the structure in fibre form than for the preform alone). The end of the cane was then sealed closed and a vacuum applied to the interface between the cane and tube during drawing. The vacuum allows the interface to seal sufficiently during drawing, while the sealing of the top end of the cane enforces self-pressurisation of the internal structure during drawing to keep the holes sufficiently open, as discussed above (*c.f.*, Ref. [177]).

All fibre samples were cleaved by hand using razor blades or surgical blades. With practice, practical, clean, fibre cleaves can be achieved with minimal fracturing of the end-face. Ceramic blades may be used but metal blades were found to produce the

[4]These issues of excess pressure can be alleviated by increasing the temperature of the glass or by slowing down the ram speed. Both options are restricted by practical barriers due to the glass itself (high-temperature crystallisation, say) or by more banal issues such as the time required to personally monitor the process.

most replicable results here. One can use more complicated mechanical fibre cleaving machines, but these can be quite cumbersome, especially for small and fragile soft-glass fibre samples. Hand-cleaving was preferred for this work for its efficacy and ease, paramount during the development stage of a novel fibre structure, as is the case here.

The effects of surface tension upon the offset struts is now much more apparent after drawing down the fibre than observed in the preform: every hole is significantly rounded, destroying the concentric ring nature of the initial structure (5.6, right). This is due to the fact that, as the glass becomes less viscous, the structure is distorted so as to minimise the surface tension forces (the most obvious effect is the rounding of sharp features); in essence, the structure tends towards a global minimum of potential energy inherent in the surface tension of the structure. This effect is also seen in the final fabricated silica fibre of Ref. [43], but the deformations aren't as obvious as the present soft-glass case since a relatively large number of struts were placed between each pair of layers, and since the drawing tension and temperature regime used in the drawing of such silica MOFs is far removed from that used for soft-glasses, the structure typically deforms less during fabrication. Of particular importance is to note the tendency of the struts and rings to tend towards linear alignment. This propensity for the thin features to align is exploited later (§ 5.3.2) in a refinement of the air-Bragg structure.

Fibre A has a collapsed hole in the outer cladding ring (Fig. 5.6). This is likely due to the fact that the jacket tube used had a slight curve along its length; a peculiarity of the glass properties and particular extrusion setup at the time such as an asymmetric temperature gradient across the glass billet and die region. This curvature required the cane to be slightly bent when inserting it into the jacket, putting undue pressure on one of its sides, weakening it. During drawing, this can manifest as a collapsed hole as the outer wall of the cane can break open at this weak point as the glass softens. Such a deformity, while unwanted, isn't critical and simply represents room for refining fabrication technique, rather than a fundamental design flaw.

Another fibre, Fibre B, was drawn from another piece of Preform 2, again via a cane-in-tube technique. Fig. 5.7 shows a SEM of Fibre B. The features of Fibre B are relatively thinner than Fibre A, due to refined drawing parameters from the experience of the previous drawing Fibre A; a step in the right direction, but clearly hampered by more severe issues. As for Fibre A, an outer hole collapsed during drawing, for similar reasons. The fact that the same type of hole collapsed is likely coincidental, and appears less remarkable once notices that it could have occurred at 3 other sites, identical up to rotational symmetry. More concerning is the observation that similar deformations as seen in the Fibre A are seen for Fibre B. These deformations are again due to the surface tension effects upon the offset struts of the glass during caning and fibre drawing.

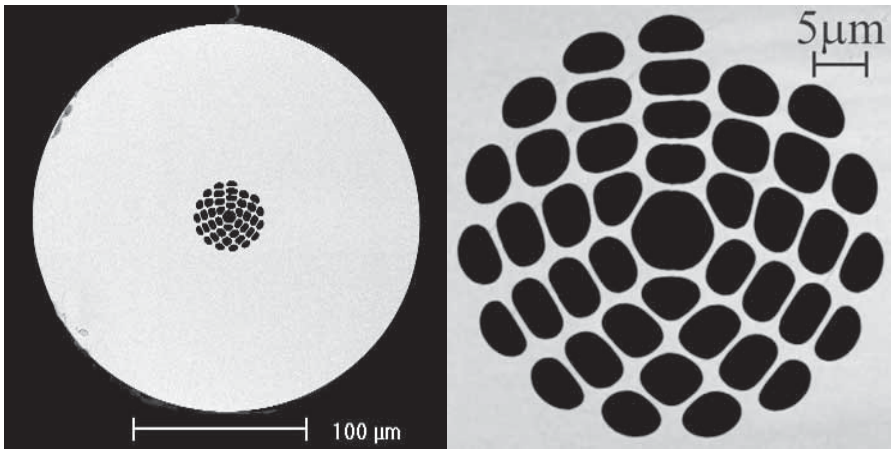

FIGURE 5.7: **Fibre B**. *Left*: A SEM of the second fabricated air-Bragg fibre using Bismuth Oxide glass. A cane-in tube technique was used after caning down a segment of the same preform used for Fibre A, Preform 2 (Fig. 5.8). As for Fibre A (Fig. 5.6), the structure is heavily deformed and a hole collapsed in the outer ring. *Right:* A magnified view of the structured region of the same fibre.

Such structural deformations will clearly destroy any 1D bandgap style guidance since the structure is no longer effectively 1D. Even if one were to argue that an antiresonant effect could produce efficient guidance, the variation in the strut and/or ring dimensions (distinguishing them becomes artificial under such severe deformations) sees that there would be a large range of resonator thicknesses, leading to a blurring together of the associated resonance transmission peaks. Finally, in retrospect the cores of these fibre samples were very small ($\approx$ 5 μm) compared to the core sizes demonstrated in the guiding silica air-Bragg fibre of Vienne et al. [43] ($\approx$ 20 μm); following the results of Chapter 2, this has the effect to significantly increase the loss, regardless of the efficacy of the resonances with the cladding structure.

Indeed, no core-guidance was observed for either Fibre 1 or 2 in the laboratory, in line with the comments above. A range of techniques were used to test for guidance. In order to merely try to observe guidance, short lengths of fibre were used to reduce the transmission losses as far as possible; 4 cm lengths were typically used, providing a reasonable trade-off between minimal length and handleability. If guidance could not even be observed in such a short length, the efficacy of the HC-MOF is questionable and the loss is assumed too large for practical guidance. The experimental methods employed to analyse the guidance behaviour of these fibres is discussed in the next section (§ 5.4).

It is clear that, in the presence of surface tension effects, the offset struts are the primary contributing factor in producing significant deformation in the fibre cross-section. The next step in the design of the soft-glass air-Bragg fibre here is to instead fabricate a fibre which works *with* the surface tension effects from its mere design. It was clear to me that the best candidate was to design the structure with *colinear* struts. As mentioned

previously, from a light guidance perspective, colinear struts have the potential to produce similar guidance properties to offset struts according to the preliminary numerical modelling in § 2.7 and the guidance properties of other HC-MOF designs in which the cladding struts are aligned such as the Kagomé-lattice HC-MOF discussed in Chapter 1. The important result of this is that the surface tension induced structural deformations of a structure with colinear struts should be confined to only rounding of the corner regions of the holes, rather than significant deformations to the ring structure. This is expected since struts in between adjacent rings would meet at common points; there would thus be no net force to 'pull' the vertices of the lattice in relatively different directions, deforming the rings. In other words, the internal forces due to surface tension during fibre drawing are more balanced for the colinear-strut case, pulling each vertex on a ring in a similar manner, reducing structural deformations.

Here I coin this air-Bragg structure with colinear struts a *spider-web* fibre, for obvious aesthetic reasons. This new structure was discussed in Chapter 1. The demonstration of its fabrication and light guidance properties are now discussed.

5.3.2 Colinear Struts—The Spider-Web Fibre

The next die design (Fig. 5.8, left) was similar to the previous two but, as discussed, employed colinear struts: every air layer contained 12 struts each, all aligned with the adjacent ring's set, effectively producing 12 long struts that cut through all the rings of the cladding. All other parameters were the same as for the previous die, except that the distance between concentric rings was a little larger (in order to increase the amount of air in the structure, aiding the self-pressurisation to produce thinner rings and struts and to reduce rounding of the features).

At this stage, the bismuth-oxide glass was replaced with a lead-silicate glass (F2, commercially available from the Schott glass company). The reasons for this change weren't so much functional as economical: the bismuth-oxide glass was not readily available as it was made available to us only through a collaboration with Asahi Glass and its availability was limited (due to the exotic nature of the glass). The lead-silicate glass, however, was readily commercially available via Schott. With respect to this particular extrusion technique, F2 is also a well-understood glass, so working with it is somewhat more straightforward than the more exotic bismuth-oxide glass. F2 has a higher softening temperature than the bismuth glass at about $590°\mathrm{C} - 600°\mathrm{C}$ and a lower refractive index of $n_{\mathrm{F2}} \approx 1.6$.

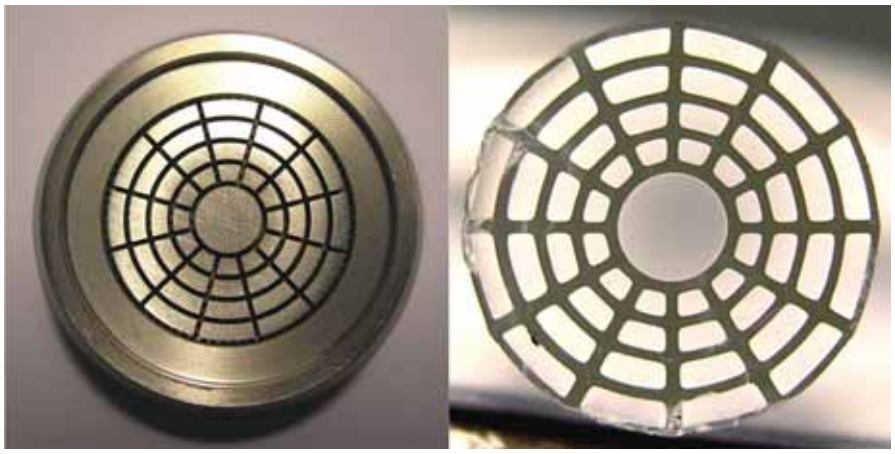

FIGURE 5.8: **Preform 3**. *Left*: Photograph of the exit-face of the stainless-steel die used to extrude a 5 cm diameter lead-silicate (F2) glass billet to create the third air-Bragg fibre preform. *Right*: Photograph of the end of the produced preform (cleaved). The diameter of this section of the preform is about 6 mm.

The preform extruded from this die, Preform 3, already demonstrates how the colinear struts work *with* the surface tension of the heated glass, better preserving the die structure than Preforms 1 and 2 of Fig. 5.4 and 5.5. The only discernible deviations of the preform structure to the die are a slight rounding of the sharp corners between the struts and rings, and a global thickening of the struts and rings (due to a common extrusion effect known as *die swell*—controllable to some extent by refining the extrusion parameters to reduce pressure on the glass [90]). The reason the surface tension doesn't disrupt the structure as it did for the previous designs is that in having the struts colinear, the surface tension forces tend to predominantly cancel out (at least locally): the forces from the rings and struts upon a particular cladding node (where the struts and rings intersect) tend to cancel each other in the azimuthal and radial directions, respectively. By not having an adjoining strut opposite a given node in the cladding, the earlier designs could not produce this force balance. The spider-web structure clearly produces the desired result insofar as minimisation of structural deformations is concerned.

Fig. 5.9 shows a scanning electron micrograph (SEM) of Fibre C pulled from Preform 3. As for the bismuth-oxide glass cases above, a cane-in-tube technique was used: the preform was first pulled down to a cane and then inserted into a hollow tube extruded from the same lead-silicate (F2) glass. The end of the cane was then sealed closed and a vacuum applied to the interface between the cane and tube during drawing to enable self-pressurisation of the holes and sealing of the cane/tube interface. As an aside, the image of Fig. 5.9 (right) was voted 'Most Beautiful Image of a Fibre' at the Workshop for Specialty Optical Fibers in Brazil, 2008.

Although significant rounding of the holes is still evident, the overall structural fidelity to both the preform and die is far superior to that observed for the offset-strut case above.

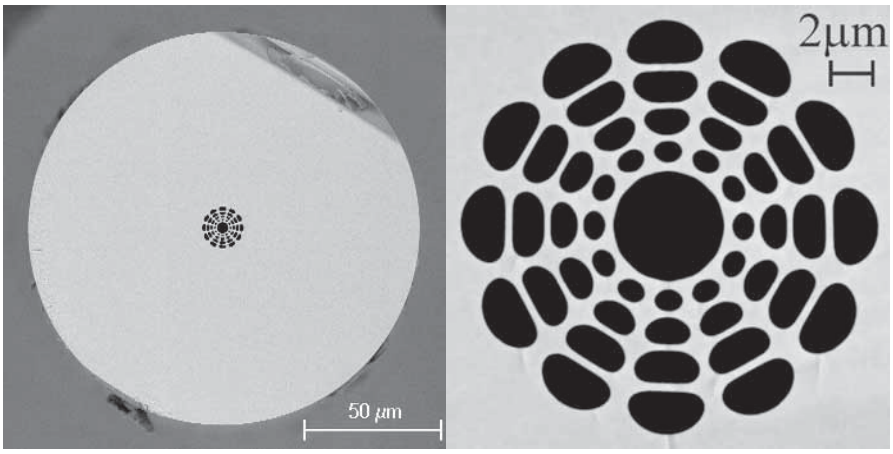

FIGURE 5.9: **Fibre C**. *Left*: A SEM of the first fabricated air-Bragg fibre using F2 glass. A cane-in tube technique was used after caning down a segment of Preform 3 (Fig. 5.8). The shown fibre segment has an outer diameter of 170 μm. *Right*: A magnified view of the structured region of the same fibre. The latter image was voted 'Most Beautiful Image of a Fibre' at the Workshop for Specialty Optical Fibers in Brazil, 2008.

The structure clearly better represents the goal of thin concentric rings supported by connective struts. It is also interesting to note the high degree of symmetry exhibited by the final fibre (12-fold, the number of struts), whereas the deformed examples above could only exhibit 3-fold symmetry due to the strut orientation (even without deformations). The enforcement of colinear struts is clearly a key step in producing a soft-glass air-Bragg fibre.

The fibre was able to be drawn down sufficiently that the rings reached the target dimensions of about 300 nm (Fig. 5.9, right); similar to the dimensions of the rings in [43]. However, at these dimensions, this particular design produces a core diameter of only approximately 4.1 μm. A core this small would increase confinement loss to impractical levels (§ 2.6). Note that the guiding fibre of Vienne et al. had a reasonably large core diameter of 20 μm. This is a fundamental design issue with the extrusion technique: only a certain number of features of a given dimension can physically fit onto an extrusion die. This makes it impossible to increase the size of a preform's air regions relative to the minimum feature size. A solution to this problem would be the alteration of the structure *after* extrusion; namely, the active inflation of the fibre structure during caning or drawing.

The inflation mechanism is quite subtle. First, consider that during fibre drawing the internal pressure of the fibre structure is actively increased. This has the effect of increasing the outer diameter of the drawn fibre while stretching the internal structure, making it relatively thinner compared to the inflated air regions. However, by increasing the drawing speed, it is possible to maintain the initial, smaller, outer diameter of

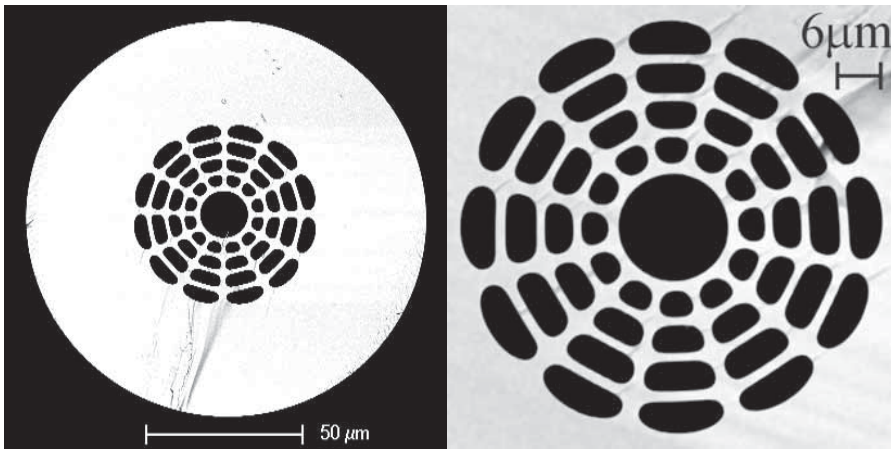

FIGURE 5.10: **Fibre** D_a. *Left*: A SEM of the second fabricated air-Bragg fibre using F2 glass. A segment of Preform 3 (Fig. 5.8) was inserted directly into a tube, rather than caning it down first. The shown fibre segment has an outer diameter of 130 μm. *Right*: A magnified view of the structured region of the same fibre.

the fibre while also pressurising it. This is because by increasing the drawing speed, the dimensions of the fibre are naturally reduced (this happens also in the absence of inflation). The underlying reason for this is the principle of conservation of mass; the material flux through a given region must be conserved. In this way, by using inflation one is able to increase the dimensions of the air:glass ratio of the structure while maintaining the same fibre outer diameter. By careful tuning of pressurisation and draw speed during fibre drawing, a broad range of inner structural dimensions are attainable. This point is returned to soon.

To see how far self-pressurisation can take the fabrication process, a second fibre, Fibre D, was drawn from another segment of Preform 3. Three samples of this fibre draw are presented here: Fibres D_a, D_b, and D_c. An SEM image of a sample of Fibre D_c in shown in Fig. 5.10. The difference with this fibre draw was that the preform wasn't caned down but inserted directly into a tube. This was possible owing to the fact that the preform itself tapered significantly under its own weight during extrusion since the furnace temperature was intentionally increased by a few $^{\circ}C$; this produced a reasonably straight region of the preform which had an outer diameter of about 6 mm, much smaller than the die exit face structure but still larger than typically possible via caning. The preform thus took the place of the cane in the cane-in-tube process.

The idea in this method was that the increased *draw-down ratio*[5] is substantially larger (larger 'cane' dimensions), increasing internal pressure at the target dimensions, thus keeping the holes open more effectively [177]. Unfortunately, the dimensions one can draw down to using this technique is restricted by the outer diameter of the jacket one

[5]The factor by which the cane-plus-jacket structure must be scaled to reach the target dimensions.

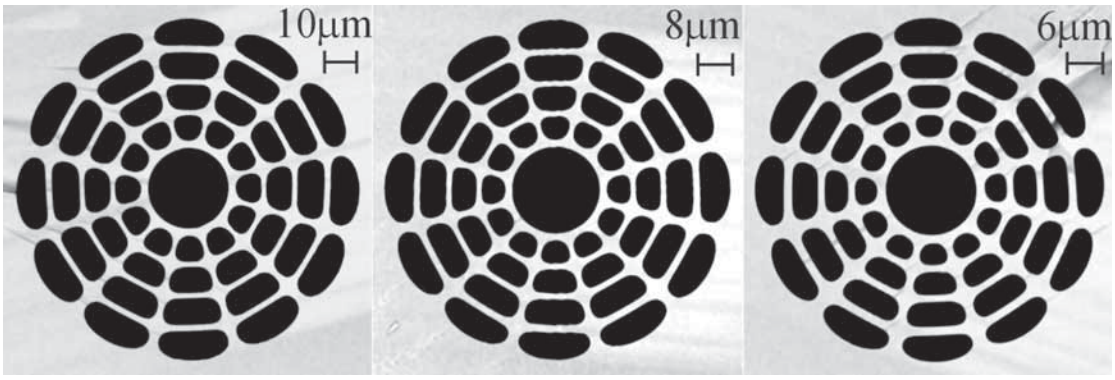

FIGURE 5.11: **Fibre D**. SEMs of Fibre D (Fig. 5.10) taken during different stages of the fibre-drawing process, producing fibres with outer diameters (left to right) 210 μm, 170 μm, and 130 μm (resp.). These fibres will be referred to, from left to right, as Fibre D_a, Fibre D_b, and Fibre D_c. Note how the features become relatively larger (the air-filling fraction decreases) as the global fibre dimensions are reduced under self-pressurisation.

can extrude; fibres with outer diameters smaller than about 100 μm become very fragile. Since the preform used is quite larger than a typical cane, the available jacket material is considerably smaller relative to the structured region (due to the finite real-estate one can exploit on a die used to make the jacket tube). Nonetheless, while the target cladding ring thickness could not be achieved (achieving a minimum of $t_{\text{ring}} \approx 1$ μm rather than ≈ 300 nm), Fig. 5.10 shows how the surface tension effects of Fibre D_a are reduced even further compared to that in Fibre C, Fig. 5.9. Take particular note of the holes closest to the core. This implies that the larger draw-down-ratio has a measurable effect upon the effective self-pressurised inflation of the structure, although repeated fabrication trials should be conducted in order to compare fibres of equal core size.

Even though the core of Fibre D_a is larger than that of Fibre C (≈ 12 μm versus ≈ 4.5 μm, respectively), no guidance was once again observed, again likely due to global confinement loss typically being very large for small core sizes (§ 2). Again, this is almost obvious in retrospect, but it was thought the ring dimensions were the most important target parameter at the time. Thin rings are most certainly not a necessary condition to simply observe guidance, as will be demonstrated presently.

Fig. 5.11 shows the cross-section of Fibre D at various stages during the drawing process, producing fibres D_a, D_b and D_c. Each sample was taken at a specific outer diameter, from larger to smaller for $D_a \rightarrow D_c$. The most obvious trend the samples demonstrate is how the surface tension effects appear to increase as the structural dimensions are decreased. This is most likely due to the increased glass flow required to reduce the structure to smaller scales; the surface tension effects have a greater opportunity to manifest under more complicated flow dynamics. Of course, this is not a sufficient

Fibre	D_{core} (μm)	t_{ring} (μm)	t_{air} (μm)
D_a	25.0	2.4, 1.7, 1.7, 2.1	8.1, 8.1, 8.3, 10.0
E	40.0	6.3, 5.4	11.6, 17.3

TABLE 5.2: Summary of selected air-Bragg fibre dimensions. Multiple entry values represent the innermost to outermost cladding features for a given structure. The measurements are to within a precision of $\approx \pm 0.2$ μm, dictated by the resolution of the SEM technique used.

explanation, but serves as a qualitative concept in the absence of a rigorous model or understanding of the fine details of the drawing of this particular HC-MOF geometry.

The structural parameters of fibre D_a as measured from the SEM image represented in Fig. 5.11 are as follows: $D_{\text{core}} \approx 25$ μm, $t_{\text{ring}} \approx [2.4, 1.7, 1.7, 2.1]$ μm and $t_{\text{air}} \approx [8.1, 8.1, 8.3, 10]$ μm, for the core diameter, inner to outer glass ring (minimum) thickness and inner to outer air gap (maximum) thicknesses, respectively. These are summarised in Table 5.2. The minimum glass ring and maximum air gap thicknesses are taken since they represent a longitudinally planar slice taken in between any two adjacent struts. The core itself if perfectly circular to within measurement error. The effects of the variations in feature sizes across the cross-section is an important consideration, but these measurements are sufficient for the discussions here.

Note that there is at least an error of ≈ 0.3 μm in these measurements of owing to the resolution of the SEM technique used. While one is justified in arguing that finer detail is required, it is a somewhat moot point in this stage of the development since the aforementioned longitudinal structural fluctuations of at least $\approx 1\%$ that occur during the fibre drawing process imply any given sample may be measurably different to the next. Measurable via SEM or not, these fluctuations have implications for light guidance along long lengths of fibre, discussed later.

While the target ring thickness parameters for this fibre design were closer to those of Fibre D_c than D_a or D_b (t_{ring} was to be as small as possible to enhance the range of any resonances, hence guidance windows), an important discovery was made: Fibre D_a *actually demonstrated observable light guidance* within the air core over a large wavelength range. This result is discussed in detail in next section (§ 5.4) together with experimental results.

Given these promising results (both in terms of structural fidelity and guidance behaviour), active inflation of this structure was also investigated. This turned out to be a highly nontrivial procedure. As discussed above, the fabrication procedure for active inflation is identical to self-pressurisation except that the cane is not sealed but sealed to a pressurised gas source. The difficult part of the process lies in achieving the ideal

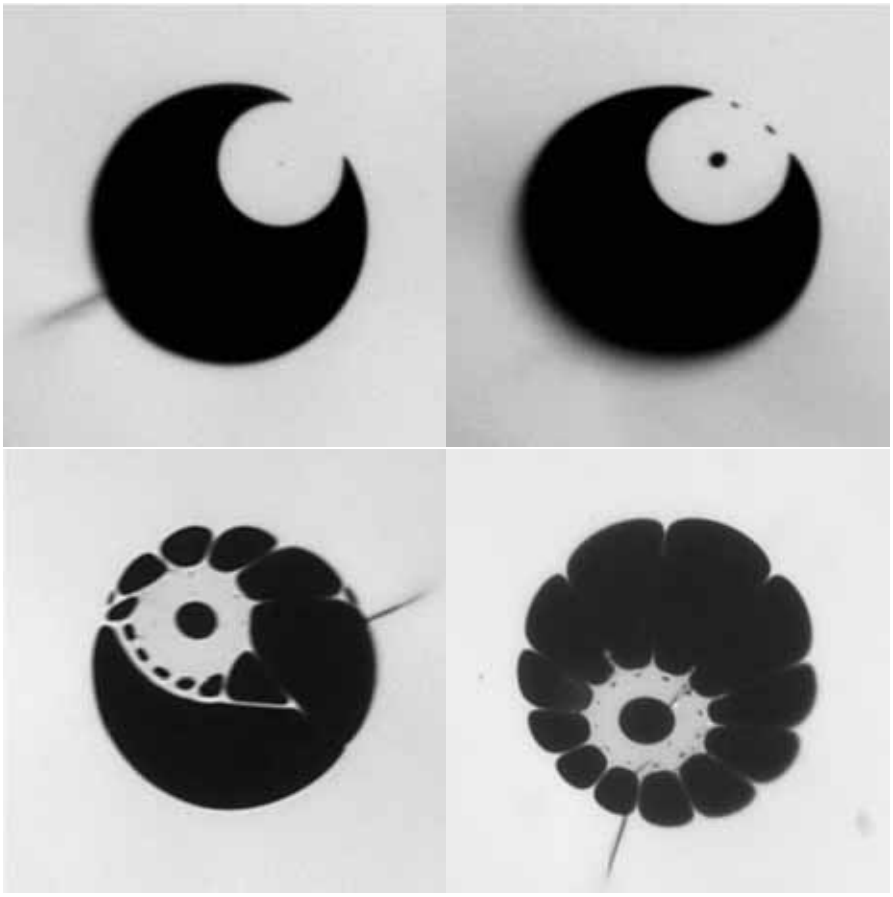

FIGURE 5.12: Optical microscope images (in reflection mode) of a failed cane-in-tube *active* inflation attempt using a cane produced from a segment of Preform 3 in which all holes are pressurised by the same amount (a common connection to the same pressure source). These undesired results imply alternative inflation techniques should be pursued to accommodate the varied sizes of the cladding holes. The extent of the structured region (the inner diameter of the jacket) is ≈ 35 μm. *Left→right*, *top→bottom:* Samples taken from sections of the fibre drawn with increasing uniform gas pressure applied to the end of the cane, demonstrating how the inflation evolved such that the larger outer holes inflate far more rapidly than the smaller ones.

drawing regime, balancing parameters such as pressurisation, draw speed and temperature. In this case, there was no vacuum applied to the cane/jacket interface under the assumption that the inflated cane would close the gap naturally (a technique regularly used for other cane-in-tube MOF fabrications).

The issue with the pressurisation of the cane in this case was that an equal pressure was applied to the entire cane structure. This saw that a greater force was applied to the outer structure walls than to the inner ones, owing to the larger outer holes. Fig. 5.12 shows the results of the inflation attempt. Without sufficient pressure, the cane collapses upon itself, forming a small solid rod stuck to the side of the inner jacket wall, Fig. 5.12

(top-left)[6]. Increasing the pressure, the holes of the cane structure begin to open to some degree, beginning with the largest hole: the core; the smaller inner holes preferentially collapsing for the above reasons. By increasing the pressure further, the outer holes balloon out until they touch the jacket wall, Fig. 5.12 (bottom-left). The core doesn't inflate to the same degree since the outer wall of the cane is relatively thin, offering the outer holes less resistance to inflation; the core has more material surrounding it that would have to be expanded in order to allow the core to inflate further. Finally, all of the out holes expand until they fill the void of the inside of the jacket (Fig. 5.12, bottom-right); no further significant inflation effects were observed after this point, although it is not clear whether increasing the pressure further would force the opening of the smaller holes as well, as is suggested by the presence of the small holes just next to the inflated outer holes in Fig. 5.12 (bottom-right).

It appears that this inflation differential across the structure prohibits this simple inflation technique from being suitable for this complex structure. In order to take the idea any further, pressurisation of the different hole types *independently* from one another may be required. This more complicated type of pressurisation technique has been successfully demonstrated for Kagomé- [9, 143] and square-lattice [160] fibre fabrication and represents a promising way forward for future work here. Alternatively, one could employ self-pressurisation (which has a propensity for maintaining structural fidelity by simply sealing one end of the cane/preform—discussed earlier) using a very large draw-down ratio so as to increase amount of inflation. It is unclear at this time whether this could be achieved to the desired scale in practice and also warrants further investigation.

An important result of this inflation trial, however, was the observation that of the holes that were inflated their walls were significantly reduced in thickness and remained intact, Fig. 5.12 (bottom-right). Indeed, the thickness of the outer struts can not be measured via the optical micrograph, implying that they must be less than ≈ 100 nm; well below the target region of $t_{\text{ring}} \approx 300$ nm. This represents a proof of principle of the inflation technique, indicating that controlled reduction in feature size should possible given the appropriate pressurisation of the holes.

Given these difficulties with inflation, it seemed clear that a larger core size was a more accessible key development to at least observing guidance in this fibre design before being able to move on to the refinement of the cladding structure, and hence guidance regimes, by techniques such as inflation. However, it has already been highlighted how the space available on the extrusion die can only accommodate a core as large as the

[6]Close inspection reveals that there is actually a very small hole in the centre of the cane, representing a near total collapse of the core.

FIGURE 5.13: **Preform 4**. *Left*: Photograph of the exit-face of the stainless-steel die used to extrude a 3 cm diameter lead-silicate (F2) glass billet creating a 2-Ring air-Bragg fibre preform with colinear struts and a *thick outer jacket*. The exit-face outer rim diameter is about 23 mm. *Right*: The fabricated preform.

extent of the cladding structure will allow. With the current cladding structure, the core size relative to the cladding extent was essentially fixed.

There were thus two primary obstacles in furthering the development of the spider-web fibre: increasing the size of the core and the inflation of the full structure. These issues were approached by changing the design of the fibre structure itself, moving to a more simple design which allows the flexibility to potentially manage these obstacles in the development of scientific validity of the fibre structure.

The new design consisted of not 4 but 2 glass cladding rings. As discussed in all previous chapters, especially §§ 2 and 3.5, at least for the idealised case without connective struts, a reduction in the number of cladding rings would decrease the minimum confinement loss achievable within a bandgap (or equivalently, at an antiresonance). This was of little concern at the time since a reduction in confinement loss represents a refinement to the waveguide; simply demonstrating resonant guidance as a proof-of-principal was more important.

The removal of two of the rings allowed the integration of a thick jacket into the die design. The manufactured die is shown in Fig. Fig. 5.13 (left); note that here that a 3 cm billet design was used, requiring smaller die dimensions compared to those used previously which were designed to accommodate 5 cm glass billets. The reduction in total die area implies a reduction in the amount of detail that can be manufactured onto the die (again, limited by feature sizes of about 0.6 mm), but this is of little concern since it is the relative, not absolute, structural feature sizes that are important when the preform is drawn down to fibre. With in integrated jacket, the cane-in-tube method could be avoided since the preform would already have sufficient jacket material to

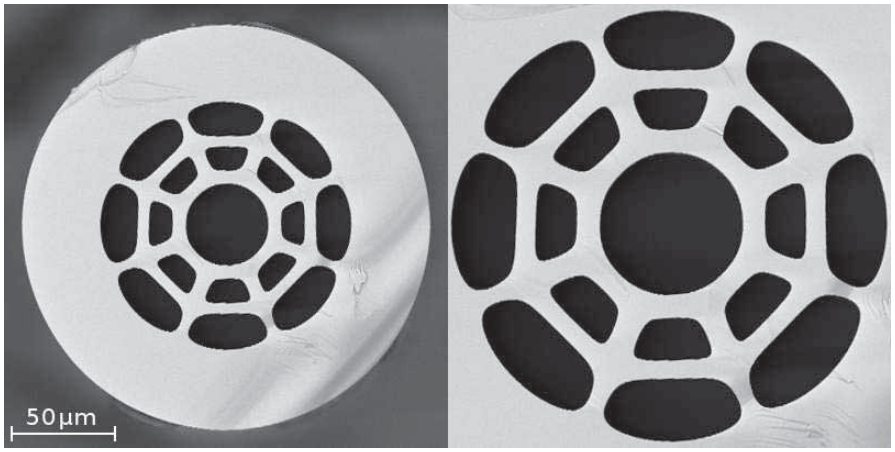

FIGURE 5.14: **Fibre E**. *Left*: A SEM of the third fabricated air-Bragg fibre using F2 glass made by directly drawing down Preform 4, sporting 2 glass cladding rings allowing an integrated jacket. The shown fibre segment has an outer diameter of $\approx$ 200 μm. *Right*: A magnified view of the structured region of the same fibre.

ensure the drawn fibre was structurally robust. Fig. 5.13 shows the preform, Preform 4, fabricated using the new die design. By drawing Preform 4 down to fibre, the final core diameter would be much larger than that available using the previous designs[7]. The trade-off is that the cladding rings would be much thicker than those achieved by Fibres A→D since, even though they were of similar size on the die, the draw-down ratio is not as large for the new design due to the thinner, but integrated (hence more easily fabricable), jacket.

With thicker cladding rings, only higher-order resonances would be accessible to the wavelength range of interest (visible to the NIR). This is immediately derived from the antiresonance condition used above in that the order of the resonances is a coefficient of the inverse of the ring thickness—from Eq. 2.4: $\lambda \propto m/t_{\text{ring}}$. That higher-order resonances are dominant is demonstrated experimentally in the next section and theoretically in the next chapter.

The integration of the outer jacket in this manner also has the potential to stabilise the inflation of the fibre structure. The ballooning out of only the outer ring of holes in the 4-ring structure above was principally due to the thin wall of the pressurised cane. With a thicker wall built into the structure by default, it could be expected that the internal structure would inflate under more control. Indeed, this was attempted during the drawing of this Preform 4, but no obvious inflation effects were observed. This could be due to insufficient pressure being used, the jacket being too thick, the draw temperature being too low, a leak occurring at the seal of the pressurised gas source to the preform, or other similar reasons; further investigation is clearly required in order

[7] A similar draw-down ratio could be achieved using the previous cane-in-tube technique using a very thin jacket tube, which has its own fabrication difficulties.

to optimise the process. Nonetheless, the fibre produced from the drawing of Preform 4 exhibited remarkable structural and optical properties, in particular the latter (as will be discussed in § 5.4).

An SEM image of a sample of Fibre E in shown in Fig. 5.14. $D_{\text{core}} \approx 40\ \mu m$, $t_{\text{ring}} \approx [6.3, 5.4]\ \mu$m and $t_{\text{air}} \approx [11.6, 17.3]\ \mu$m, for the core diameter, inner to outer glass ring (minimum) thickness and inner to outer air gap (maximum) thicknesses, respectively. These are summarised in Table 5.2. The minimum glass ring and maximum air gap thicknesses are taken since they represent a longitudinally planar slice taken in between any two adjacent struts. The core itself is approximately circular to within (has elliptical semi-axes that differ by) $< 1\ \mu$m, beyond the resolution error of $\pm 0.3\ \mu$m. The effects of the variations in feature sizes in the transverse cross-section is an important consideration, but these measurements are sufficient for the discussions here. Longitudinal variations along the fibre length are quite important and discussed in more detail soon with respect to their effect on transmission spectra for various fibre lengths.

Of most importance for these results is that Fibre E, the 2-ring spider-web fibre, like the 4-ring Fibre D_a above, exhibits light guidance within the core. More than this, the transmission spectrum clearly implies a strong resonant guidance mechanism. These experimental results are now presented and discussed.

5.4 Hollow-Core Guidance—Experimental Results and Antiresonance Analysis

In order to first test a given fibre sample for guidance within the hollow core (regardless of guidance mechanism), short lengths of fibre were used to reduce the transmission losses as far as possible; 4 cm lengths were typically used, providing a reasonable trade-off between minimal length and handleability. If guidance could not be observed in such a short length, the efficacy of the HC-MOF was deemed questionable and the loss was assumed too large for practical guidance and hence of little use for diagnostics.

The first test for light guidance involved simply mounting a short sample of fibre (hand-cleaved using a razor blade) on an optical microscope in transmission mode such that the condenser lens focuses the incandecent lamp's light as tightly as possible upon the end face of the short fibre sample. With sufficient alignment of the sample, one can efficiently couple light into the guiding structures of a fibre.

For measurements of a fibres transmission spectrum, a supercontinuum white light source[8] was coupled into the fibre in a similar manner, except appropriate fibre mounts (micro- and nano-positioning stages) coupling optics (microscope objectives and lenses) and detectors were used (similar to § 4—sans the filling apparatus). After aperturing off the small amount of light coupled into the cladding (due to unavoidable in-coupling, inter-mode coupling or scattering effects), the core light was free-space coupled input into an optical spectrum analyser (OSA).

[8] A SuperK^{TM} Compact from the commercial photonics company Koheras, now a part of NKT Photonics.

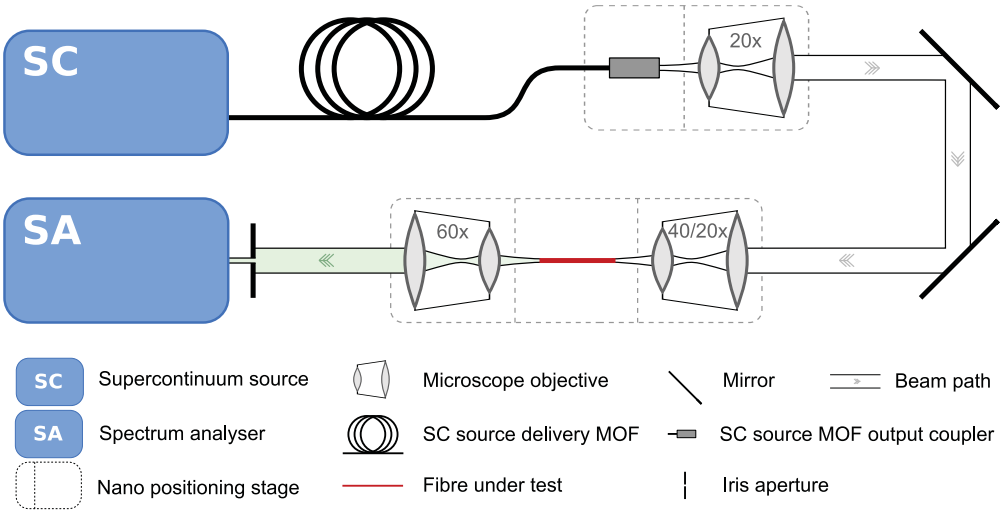

FIGURE 5.15: Spider-web air-Bragg fibre spectra measurement schematic.

A 60× microscope objective was used to focus the out-coupled light into the OSA, while either a 40× or 20× objective was used to couple into the samples of Fibre D_a or Fibre E, respectively. For samples below a length of about 10 cm, mounting each end of the fibre on an independent nano-positioning stage became impossible; only one stage was used to hold the small sample with the mount of the second (out-coupling) stage being removed so that the second objective could be placed as close as possible to the free end of the sample[9]. Figure 5.15 shows a schematic of the apparatus used including the modified combination of the positioning stages.

5.4.1 4-Ring Spider-Web Fibre—Fibre D_a

Figure 5.16 shows an optical microscope image in transmission, demonstrating the guidance properties of Fibre D_a in the visible region. The over-exposed appearance of the cladding structure is due to the poor in-coupling of the incandescent lamplight of the microscope into the fibre; the condenser lens only has a finite focal length and working distance, so the resulting large spot-size illuminated much of the cladding as well as the core. In the laboratory, with the appropriate optical equipment, minimal coupling to the cladding is achieved. The experimental results of this guidance are discussed in the next section and, in particular, whether the guidance exhibits any resonant behaviour with the cladding structure.

Now, suspicion was immediately drawn to the possible dominance of simple 'capillary' guidance, a result of Fresnel reflection from only the core interface (just as for the tube waveguide of § 2.3.1). Capillary dominated guidance in polymer HC-MOF trials due to insufficient structural integrity in the cladding was reported by Ref. [95]; the principle could potentially apply here, too. Capillary guidance, as discussed in § 2.3.1 and Ref. [95], produces confinement loss that increases monotonically with λ (transmission spectrum increased for decreasing λ); the normalised transmission spectrum of such a waveguide asymptotically approaches 1 for decreasing λ. While this tendency for the transmission to increase (loss decrease) toward shorter wavelengths, the important observation for the fibre at hand was that *a rich variety of strong spectral features was observed within this trend.* This spectral structure and its, origin is now discussed.

Fig. 5.17, shows the transmission spectrum of Fibre D_a as measured using the supercontinuum source as described above. Fig. 5.17 shows the transmission spectra of two samples: one of length 5.8 cm (top) and the other of 4 cm, measured with an OSA wavelength resolution of 5 nm and 1 nm, respectively (a 5 nm resolution version of the

[9]This practice could be a problem for small-core fibres, but the dimensions of the spider-web fibres used here are large enough such that one can afford to be a little more lax with the precision of the out-coupling optics.

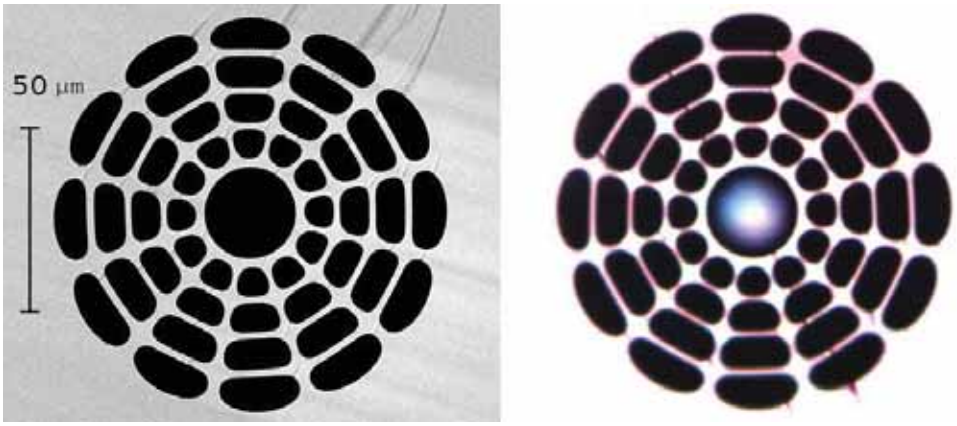

FIGURE 5.16: SEM (*left*) and transmission microscope (*right*) images of Fibre D_a.

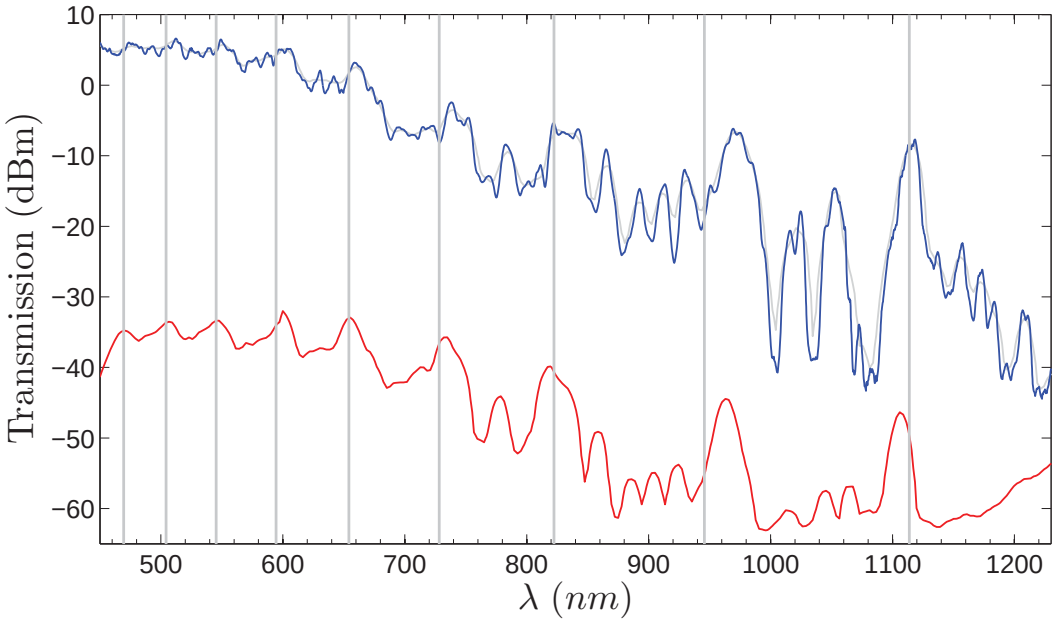

FIGURE 5.17: Transmission power spectrum of Fibre D_a normalised to the source spectrum. *Blue:* A 5.8 cm long sample with the spectrum measured to a 1 nm resolution. *Light grey:* The same spectrum measured with 5 nm resolution. *Red:* A 4 cm sample measured at 5 nm resolution, artificially vertically offset from the first sample for ease of representation. Note the alignment of the major peaks between the two samples.

latter also overlayed on the same plot—light grey). The lower spectrum is artificially vertically offset from the first for ease of representation.

Strong resonant features are shown in the spectra for these samples of Fibre D_a. This is a significant departure from the smooth asymptotic behaviour one would expect were the light not experiencing a strong resonant interaction with the cladding; as demonstrated experimentally by Argyros et al. using a hexagonal-lattice polymer HC-MOF design, the lack of a resonant interaction with the cladding produces guidance similar to a simple tube [95].

F2 Schott Glass Sellmeier Material Dispersion Fit

Formula	$n_{\mathrm{F2}}(\lambda) = \sqrt{1 + \Sigma_i B_i \lambda^2/(\lambda^2 - C_i)}$		
Coefficients	B_1	B_2	B_3
	1.34533359	0.209073176	0.937357162
	C_1	C_2	C_3
	0.00997743871	0.0470450767	111.886764

Sample calculations

λ (μm)	n_{F2}		
0.35	1.6742	...	
0.4	1.6522	1.0	1.6031
0.45	1.6388	1.2	1.5996
0.5	1.6299	1.4	1.5968
0.6	1.6190	1.55	1.5949
0.7	1.6126	1.6	1.5943
0.8	1.6084	1.8	1.5918
0.9	1.6054	2.0	1.5892
...		2.3	1.5850

TABLE 5.3: Sellmeier formula, empirically derived coefficients and selected values for the F2 glass from Schott used in this work. Coefficient values taken from the official Schott F2 glass datasheet; applicable at least for the range $\lambda = 334.1$ nm $\rightarrow$ 2325.4 nm. A selection of refractive indices are also calculated from the Sellmeier formula are also given, covering the visible to the NIR spectrum. Values of n_{F2} truncated to 5 significant figures.

A critical observation here is that *these spectral peaks* (Fig. 5.17) *closely correspond to the antiresonance conditions one expects from the cladding structure!* This is shown in Fig. 5.17 by the alignment of the measured transmission peaks with the antiresonance wavelengths represented by the array of vertical grey lines. These lines actually correspond to the antiresonance conditions of the *first cladding ring* which, as per Table 5.2, has a thickness of $t_{\mathrm{ring},1} \approx 2.4$ μm. Were one to ignore the material dispersion of the glass, the antiresonance conditions could be evaluated directly from the ARROW resonance condition of Eq. 2.4, with antiresonances corresponding to half-integer resonance orders $m = \frac{1}{2}, \frac{3}{2}, \ldots$, as discussed in § 2.3.3. These half-integer m^{th} order resonances will be referred to here as the antiresonance orders $\overline{m}$ which a related to the resonances as $\overline{m} = m + \frac{1}{2} = 1, 2, \ldots$

In order to compare these antiresonance wavelengths with the experimentally measured transmission spectra here, however, the material dispersion of the glass must be explicitly considered. To do this I have employed the Sellmeier refractive index dispersion fit; a Sellmeier function is an empirically derived fit (to terms of inverse powers of wavelength) to many precisely measured data-points of the glass refractive index, allowing the calculation of a well-defined approximation to the glass index at any wavelength

within the fit's range of applicability ($\lambda = 334.1$ nm $\rightarrow$ 2325.4 nm here, according to the official Schott F2 datasheet). The Sellmeier formula and coefficients used are shown in Table 5.3 with a selected range of calculated indices listed as a reference.

In enforcing a wavelength dependent refractive index, the antiresonance condition of Eq. 2.4 is *no longer analytic*. One must then solve the antiresonance condition numerically. This has been done here by finding the roots (with respect to λ) of the Sellmeier-based antiresonance expression (derived from Eq. 2.4):

$$\frac{2t}{m}\sqrt{n_{\mathrm{F2}}(\lambda)^2 - n_0^2} - \lambda = 0, \tag{5.2}$$

where $n_{\mathrm{F2}}(\lambda)$ is the polynomial Sellmeier function of Table 5.3 and the second refractive index is assumed constant (a good assumption for air and many liquids relative to the glass). For a given m and t, there is one root for this equation, λ_m^{AR}. The grey vertical lines of Fig. 5.17 represent the antiresonances calculated using this method in which $t = t_{\mathrm{ring},1} = 2.45$ μm and $\overline{m} = 6 \rightarrow 14$ (lowest orders correspond to the longest wavelength and vice versa).[10] The values of the inner ring antiresonance wavelengths including material dispersion are summarised in Table 5.4.

The incorporation of material dispersion is critical when comparing with the experimental results as can be evidenced by noting that, when one does the substitution in the calculations, resonance shifts of up to a whole order are possible when replacing the Sellmeier glass index with a constant value. These differences between the resonances for incorporated and ignored material dispersion are also non-uniform in λ due to the nonlinear nature of the Sellmeier fit. The paramount importance of incorporating material dispersion was also demonstrated explicitly in the experimental and theoretical analysis of liquid-filled Bragg fibres earlier in § 4.

The observed spectral peaks thus correspond to the 6^{th} to the 14^{th} antiresonances of the first glass cladding layer. Note that this agreement is observed in spite of the subsequent glass rings having substantially varying thicknesses which would produce quite different resonance wavelengths. This is of little surprise given that, as discussed by many other works (*e.g.* [9, 99, 100, 149]), the innermost layers have a dominant influence over the reflectivity of the cladding structure since the electromagnetic fields of the guided light are largest there, decaying as they penetrate the structure towards the subsequent rings (as demonstrated for the idealised air-Bragg structure in Fig. 2.7).

The measured spectral peaks don't appear to be regular, however. This is likely due to one of two reasons. First that the varying thicknesses of rings in the cladding, Table 5.1,

[10] This value for the inner ring thickness differs to that listed as the measured thickness by 50 nm ($\approx 2\%$), within the fabrication and measurement error tolerances mentioned above.

Fibre D_a ($t_{\text{ring},1} = 2.45$ μm)

$\overline{m}$	$\lambda_{\overline{m}}$ (nm)	n_{F2}	$S^{\%}_{\overline{m},\overline{m}+1}$	$\Delta^{\%}_{S}\lambda_{\overline{m}}\vert_{S=0.99}$
6	1113.8	1.6010	15.0982	6.4980
7	945.66	1.6043	13.0354	7.5033
8	822.39	1.6076	11.4422	8.5082
9	728.29	1.6112	10.1723	9.5130
10	654.21	1.6152	9.1339	10.5181
11	594.45	1.6195	8.2669	11.5237
12	545.31	1.6242	7.5301	12.5300
13	504.25	1.6293	6.8943	13.5373
14	469.48	1.6350	6.3382	14.5457

Fibre E ($t_{\text{ring},1} = 6.3$ μm)

$\overline{m}$	$\lambda_{\overline{m}}$ (nm)	n_{F2}	$S^{\%}_{\overline{m},\overline{m}+1}$ (%)	$\Delta^{\%}_{S}\lambda_{\overline{m}}\vert_{S=0.99}$ (%)
17	957.67	1.6040	5.5904	17.502
18	904.14	1.6053	5.2793	18.503
19	856.41	1.6066	4.9991	19.505
20	813.59	1.6079	4.7453	20.506
21	774.99	1.6093	4.5142	21.508
22	740.00	1.6107	4.3029	22.509
23	708.16	1.6122	4.1089	23.511
24	679.06	1.6137	3.9301	24.512
25	652.37	1.6153	3.7646	25.514
26	627.82	1.6169	3.6110	26.516
27	605.14	1.6186	3.4680	27.517
28	584.16	1.6203	3.3345	28.519
29	564.68	1.6221	3.2095	29.520
30	546.56	1.6240	3.0921	30.522
31	529.66	1.6260	2.9817	31.524
32	513.86	1.6280	2.8776	32.526
33	499.08	1.6301	2.7791	33.528
34	485.21	1.6322	2.6859	34.530

TABLE 5.4: Antiresonance wavelengths for F2 glass layers incorporating material dispersion corresponding to the inner rings of Fibres D_a and E (inner layer thicknesses taken from Table 5.2). The refractive indices corresponding to the antiresonance wavelengths are also listed (calculated from the Sellmeier material dispersion fitting function of Table 5.3.). $S^{\%}_{\overline{m},\overline{m}+1} = (1 - S_{\overline{m},\overline{m}+1}) \times 100$. $\Delta^{\%}_{S}\lambda_{\overline{m}} = \Delta\lambda_{\overline{m}}/(\lambda_{\overline{m}} - \lambda_{\overline{m}+1}) \times 100$. Values are truncated to 5 significant figures. The antiresonances listed correspond to those shown in Figs. 5.16, 5.18 and 5.21.

produce misaligned (but coupled) resonances with the fields of the guided core light, contributing to the total transmission spectrum—where many of the antiresonance peaks of the layers align, large peaks in the transmission spectrum would be observed. The dips in the spectrum could also possibly be due to strong couplings of the core modes to the cladding modes supported in the glass web or holes.

The first phenomenon, that of misaligned and coupled resonances producing the variety of spectral features, is analysed numerically in the next chapter using the FEM introduced in § 2.3.4 and used in §§ 2 and 3.6.

The latter phenomenon might not be such a great concern following the discussions of the works of Ref. [9, 142, 145, 159] (discussed in § 1.2.3) where it has been shown how coupling to cladding modes is far less significant than the resonances with the cladding struts in Von Neumann Wigner guiding HC-MOFS such as the Kagomé- and square-lattice fibres. The spider-web fibre shown here has many similarities to such fibres, including a large cladding pitch which is attributed to suppression of such core/cladding mode interactions [9, 142, 145, 159]. Furthermore, it is clear from the microscope images in transmission mode, that the cladding guides light efficiently in both its glass regions and holes when light is couple to them. This suggests the absence of a cladding bandgap but, from the core mode transmission spectra above, clearly the existence of an antiresonance guidance mechanism for the core mode. The spider-web fibre thus likely also guides via a Von Neumann Wigner mechanism, similar to that demonstrated in waveguides such as the Kagomé fibre above (the core mode loss spectrum is dominated by the cladding resonances, coupling only very weakly to the cladding modes themselves—Chapter 1, Fig. 1.7). Of course, further theoretical and experimental investigation is required to be sure of it.

Note how the major transmission peaks observed from each sample in Fig. 5.17 are aligned with the other sample's. This implies that there is a good stability in the structural dimensions from sample to sample. As discussed earlier, instabilities during the fibre drawing process could disrupt the longitudinal stability of a given structural feature (changing the size of a hole or ring thickness, say). Since resonant interactions with the cladding structure are very sensitive to the cladding feature dimensions, stable fibre drawing conditions are paramount for fibres such as these. If there were a strong diameter variation along the length of the fibre, say, the high-loss spectral features of the cladding would vary along the length, too, such that the observed transmission spectra of sufficiently long lengths of fibre would have their resonant features 'washed out' due to the integrated effect of the various spectral features generated along the length of the fibre. The fact that the peaks appear consistent between samples here implies that the unavoidable $\sim \pm 1\%$ outer-diameter variation under the fibre fabrication technique used

here doesn't translate to significant changes of the internal structure. It is likely that the structural fluctuations thus induce a global scaling, fluctuating the cladding rings by the same relative scale. The repercussions of this are discussed in detail later.

From carefully measured transmission spectra, one can derive the loss spectrum of the fibre. The loss spectra are calculated by considering a specific wavelength and the associated fibre sample length and transmission power values. A linear least-squares fit to the data points of power versus sample length is calculated. The slope of this linear fit represents the average power difference measured across all samples for that wavelength, hence the loss per unit length. Repeating this for all wavelengths produces a transmission loss spectrum.

Figure 5.18 shows two of the transmission spectra (top) measured from samples ranging from lengths $L = 11$ cm $\rightarrow 5.8$ cm± 0.5 mm used to calculate the loss spectrum (bottom) of a sample of Fibre D_a. Only the wavelength range 450 nm $\rightarrow$ 700 nm is considered as the fibre was too lossy for longer wavelengths using longer lengths of fibre and the transmission spectrum is limited by the sensitivity of the OSA. Without an accurate reading for such low power levels, the data would skew the loss calculations, so they are thus omitted.

One can see how spectral features which otherwise might not appear obvious from the transmission spectra alone become more apparent when the loss is measured. In particular, note the existence of clear loss minima dips which are surrounded by multiple less pronounced minima. These minima correspond precisely to the transmission peaks in Fig. 5.18, as one would expect: the spectral features corresponding to the lowest loss produce the highest transmission peaks over a given length of fibre.

More importantly, as for the transmission peaks, the principal loss minima have an excellent correspondence with the calculated antiresonances of the first cladding ring (grey vertical lines, Fig. 5.18). The transmission peaks and loss minima shown in Fig.5.18 thus correspond to inner-ring resonances of order $\overline{m} = 6 \rightarrow 14$.

Note how the behaviour describe theoretically in § 2.4 is observed in these loss spectra: higher-order antiresonances produce guided modes of lower loss (following a predominant downward trend in a similar manner to the tube waveguide equivalent). It is unclear as to what the precise modal content of the guided light is for the transmission measured here for Fibre D_a, although it is likely that it is dominated by the HE_{11} owing to asymptotic single-modedness [39, 43, 63, 65, 171] and the fact that the optical micrograph of Fig. 5.16 suggests a Gaussian-like transverse intensity distribution (similar to the HE_{11} mode). Further investigation is required in both the experimental and theoretical analysis of these fibres to determine the behaviour and influence of the mode content further.

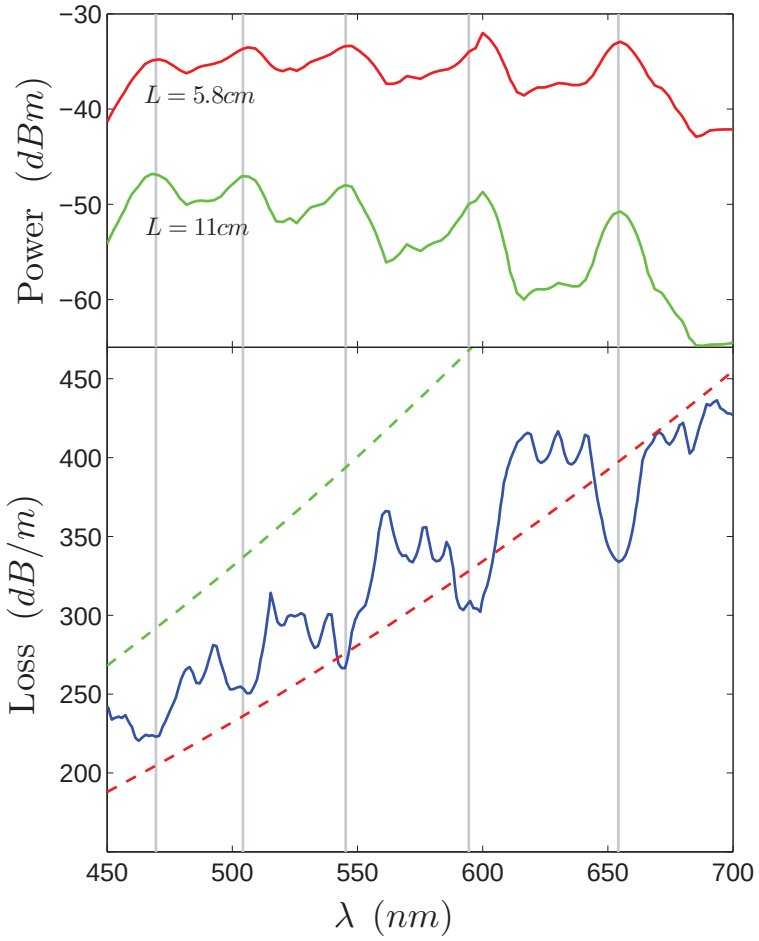

FIGURE 5.18: *Top:* The transmission power spectra, normalised to the source spectrum, measured for a sample of Fibre D_a for the longest (*solid red*, $L = 11$ cm) to shortest (*solid green*, $L = 5.8$ cm) lengths used in the cut-back loss measurement. *Bottom:* The transmission loss curve (*blue*) calculated from a series of transmission curves from a sample cut back over a range of lengths: $L = 11$ cm $\rightarrow 5.8$ cm. *Grey vertical lines:* antiresonance wavelengths for the inner cladding ring, incorporating material dispersion, taken from Table 5.4. Note how the loss minima and transmission maxima are aligned with the calculated antiresonance wavelengths. Modal confinement loss curves of equivalent tube waveguides (same 25 μm core diameter but with an infinite homogeneous cladding) are overlayed; *Dashed red:* HE_{11}, *Dashed green:* TE_{01}.

Fig. 5.18 also compares the measured loss spectrum to the equivalent tube waveguide ($D_{\text{core}} = 25$ μm with an F2 glass cladding). The asymptotic analytic approximation for the modes of a tube guide presented in § 2.3.1 and derived in § A.4.3; the large core diameter ensures the asymptotic approximation is valid (§ A.4.3). The dashed curves represent the confinement loss of the lowest order modes of the tube guide (HE_{11} and TE_{01}). The HE_{11} mode thus represents the minimum theoretical loss of a perfect tube waveguide. As for the antiresonance calculations above, the full chromatic dispersion of the glass is considered when calculating the tube modes' CL by employing the Sellmeier refractive index function of Table 5.3.

Note that the material loss of the glass is negligible for the wavelengths considered. For example, according to the official Schott F2 glass datasheet, the internal transmittance of a 25 mm sample of F2 glass is about 0.997 over the visible spectrum, corresponding to a bulk optical loss of about 0.5 dB/m, which is well below the transmission losses measured for all fibre samples considered here. Similarly, the bulk transmittance for wavelengths into the NIR like, say, 1.55 μm is stated as 0.989, corresponding to a bulk optical loss of about 2 dB/m. Since the majority of the light is guided within the hollow core of these fibres, assuming a generous mode-field/material overlap of about 10%, the loss attributed to the glass would be at least less than 0.2 dB/m. When comparing this material absorption loss to the total loss of the current fabricated fibres ($\sim$ 100 dB/m, *e.g.* Fig. 5.18, and Fig. 5.21 later), for all intents and purposes the glass can be approximated to be transparent for the wavelengths used here; confinement loss and structural scattering features (such as surface capillary waves or similar surface roughness) are considered the dominant loss mechanisms. Indeed, following refinements to the design and fabrication of these fibres, the goal would be to reduce the confinement loss as far as to make the material loss an appreciable fraction of the transmission loss, thus reducing the problem to material engineering rather than optical design.

5.4.2 2-Ring Spider-Web Fibre—Fibre E

Figure 5.19 shows an SEM and transmission microscope image of Fibre E. A significant amount of light is clearly guided within the core with an apparently white appearance. As for Fibre D_a, the microscope image was created by focusing the microscope lamp onto the fibre end-face, coupling as much as possible into the core—since the condenser lens of the microscope isn't designed for this, coupling a significant amount of light into the cladding is unavoidable, resulting in the coloured appearance of the cladding structure and some weak guidance in the outer cladding holes (permitted due to the Von Neumann Wigner nature of the guidance mechanism). When coupling light into the fibre on the optical table (as in Fig. 5.15), the cladding light is greatly diminished.

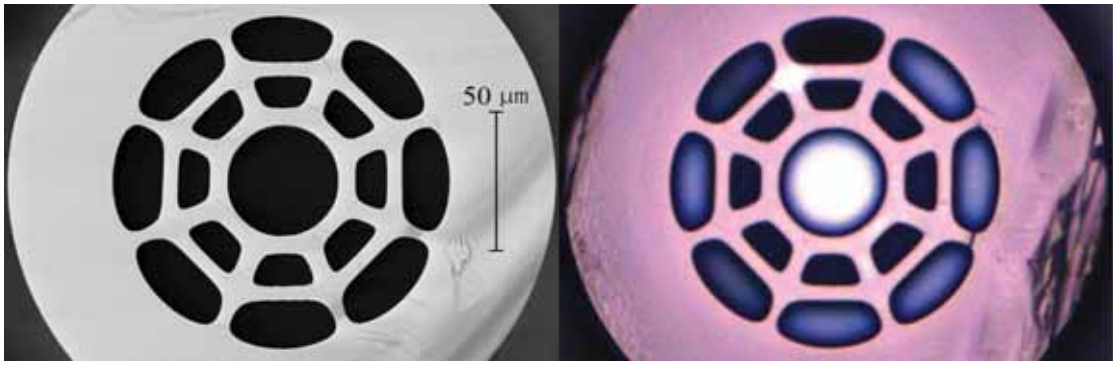

FIGURE 5.19: SEM (*left*) and transmission microscope (*right*) images of Fibre E.

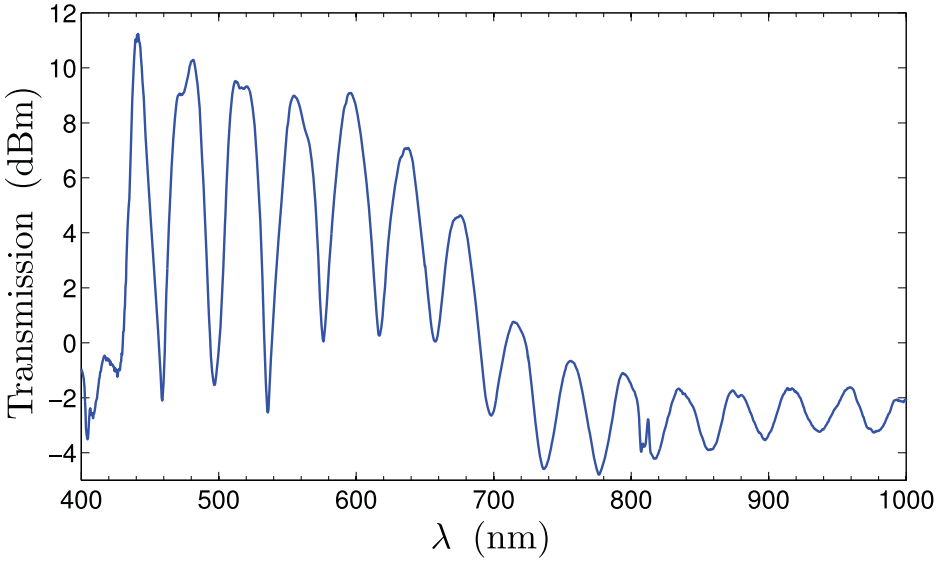

FIGURE 5.20: Transmission power spectrum of Fibre E, normalised to the source spectrum. The spectrum was measured using a ≈ 5 cm long sample and a spectral resolution of 1 nm. Note the regularity of the peaks with almost no sub-peaks or disruptions to the spectrum. These transmission peaks do not align with the antiresonance wavelength of the cladding rings—discussed further in the text.

The transmission spectrum of a short length (≈ 5 cm) of Fibre E is shown in Fig. 5.20. Note the regularity of the peaks with almost no sub-peaks or disruptions to the spectrum as was observed for Fibre D_a. These transmission peaks are very strong and much more obvious than those of Fibre D_a. The peaks are clearly more numerous than those of Fibre D_a, though, which is entirely due to the larger cladding ring thicknesses producing a larger number of resonances over the same spectral range; recall the antiresonance condition requires $\lambda_m \propto t/m$ such that thicker rings will produce more (higher-order) resonances over a given spectral region. This explains the white appearance of the core light: the many transmission peaks over the visible spectrum conspire to give the appearance of white light.

Figure 5.21 shows the transmission spectra of a range of lengths of Fibre E. Note how the transmission peaks, as for Fibre D_a above, align with the calculated antiresonances (which include materials dispersion—their values are listed in Table 5.4). All measured transmission peaks, that is, except for those of the shortest sample shown. The 4.18 cm long sample, whose transmission spectrum was shown more clearly in Fig. 5.20, does not exhibit peaks that align with the calculated antiresonances and don't appear to even align with integer fractions of them, either.

It is likely that this anomalous behaviour for the short lengths is an artifact of multi-mode guidance. Over such a short propagation distance, higher-order modes may not have accumulated sufficient loss in order to be discriminated sufficiently from the lowest order modes (as per the discussions of asymptotic single-modedness in Chapter 1, say). With the current fibre designs, confinement loss would be the predominant asymptotic mode discrimination mechanism (since it is likely the largest loss mechanism, as discussed). This asymptotic loss explanation is backed-up by the observation that these transmission peaks decay quickly as the length of the sample is increased (Fig. 5.21). However, this decay effect could also be due to the accumulation of losses due to fabrication imperfections (scale fluctuations, say) along the length of the fibre, which is discussed in far more detail presently.

Either way, the 4.18 cm length sample certainly produces the most regular transmission peaks with a large peak-to-trough height. Incidentally, it was observed that these peaks were very sensitive to coupling alignment and even to small disturbances to the fibre such as applying pressure to the jacket (being careful not to disturb the alignment). This suggests that this higher-order core mode resonance behaviour could find an unexpected application to strain sensing, for example, although further investigation is required.

This anomalous short-length behaviour aside, the transmission spectra of Fig. 5.21 (top) show that the transmission of Fibre E is quite similar to that of Fibre D_a in that the transmission peaks align with their calculated inner-ring antiresonances. In this

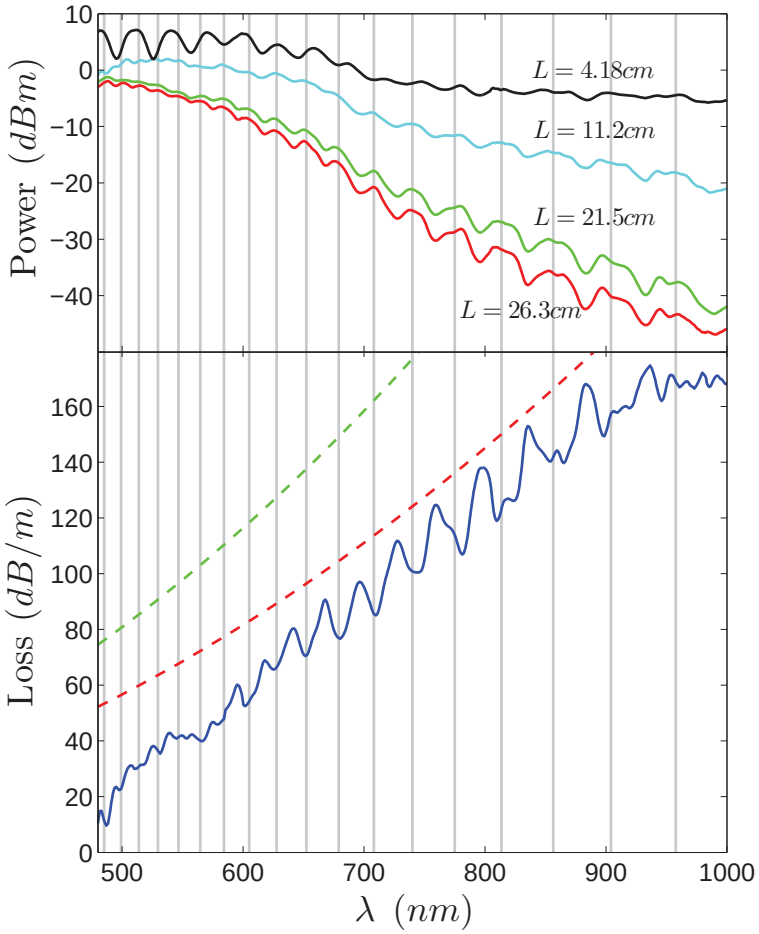

FIGURE 5.21: *Top:* The transmission power spectra, normalised to the source spectrum, measured for a sample of Fibre E for the longest (*solid red*, $L = 26.3$ cm) to shortest (*solid green*, $L = 4.18$ cm) lengths used in the cut-back loss measurement. *Bottom:* The transmission loss curve (*blue*) of Fibre E calculated from a series of transmission curves from a sample cut back over a range of lengths: $L = 26.3$ cm $\rightarrow 11.2$ cm (the 4.18 cm sample is neglected). *Grey vertical lines:* antiresonance wavelengths for the inner cladding ring, incorporating material dispersion, taken from Table 5.4. Note how the loss minima and transmission maxima are aligned with the calculated antiresonance wavelengths. Modal confinement loss curves of equivalent tube waveguides (same 40 μm core diameter but with an infinite homogeneous cladding) are overlayed—*Dashed red:* HE_{11}, *Dashed green:* TE_{01}.

longer length regime, then, it appears that the inner ring is once again predominantly responsible for the antiresonance behaviour—investigated further via a full numerical analysis in § 5.5. Taking the measured transmission spectra for a range of sample lengths, such as those shown in Fig. 5.21 (top—excluding the shortest sample as discussed), one can calculate the transmission loss spectrum using the same method as discussed for Fibre D_a earlier. Fig. 5.21 shows this loss spectrum, comparing it to the losses one would expect from the lowest order modes of a simple tube.

As for Fibre D_a, Fibre E demonstrates the general trend of decreasing loss with decreasing wavelength following the trend of the tube modes. Once again, one observes that on top of this trend are superposed strong resonance-based loss dips. This is a significant observations, implying that even with cladding ring and struts features as large as those of Fibre E, and with as few layers, resonance effects are still easily observed. These results indicate that there is great merit in refining the design to produce structures of thinner cladding features in order to widen the low-loss bandwidths (by further separating the resonances) and at the same time decreasing their minimum achievable confinement loss. This last comment may appear at odds with the work of Chapter 2 in which it was shown that higher-order resonances produce lower CL. However, it must be appreciated that the inclusion of such large struts into the structure has a significant in increasing its loss (demonstrated in the numerical results in § 5.5). Furthermore, as shown in Table 5.4, the resonances of Fibre E are very high order (up to $m = 34$ for those in the spectrum shown here). These very high-order resonances are more susceptible to structural deformations than lower-order resonances, increasing the total loss of a length of fibre. This effect can already be seen in the transmission and loss spectra of Fibre E in Fig. 5.21 in that the resonance effect observed flatten out towards shorter wavelengths.

Given these comments, it is clear that the implications of structural fluctuations on the guidance of Fibre E must be considered more carefully. It will now be shown how a fabrication tolerance induced scale fluctuation of $\pm 1\%$ (that of the fabrication apparatus used to draw these fibres) will shift the various resonances by different amounts, especially for higher-order resonances. This can be quantified analytically, as is now be shown.

Consider a structural scale factor S which scales the thickness t_1 of a glass layer as $t_1 \rightarrow t_1' = St_1$. Neglecting material dispersion, Eq. 2.4 implies $\lambda_m = 2t_1\Delta n/m$ for a resonance of order m (as usual, antiresonances correspond to $m = \frac{1}{2}, \frac{3}{2}, \ldots$) and geometric refractive index difference factor $\sqrt{n_1^2 - n_0^2}$. The resonance wavelength thus shifts under the layer scaling as $\lambda_m \rightarrow 2St_1\Delta n/m = S\lambda_m$. For the m^{th} resonance wavelength to shift to the l^{th} resonance wavelength, one requires a scale factor $S_{m,l}$ such that $\lambda_m \rightarrow \lambda_l = S_{m,l}\lambda_m$. The equality implies the scale factor is related only to the two resonance orders as $S_{m,l} = m/l$. The order parameter l can be considered as continuous such that λ_l can be tuned to any wavelength to which $S_{m,l}$ gives the scale factor required to shift λ_m to that wavelength. Thus, in the absence of material dispersion, the wavelength shift of a given resonance under a layer thickness scale transformation is totally independent of the structure itself and only dependent on the resonance orders one is shifting from (m) and to (l) as embodied in $S_{m,l} = m/l$.

Take the case of $l = m + 1$; larger m will thus produce lower $S_{m,l}$ as the ratio of m and $m+1$ becomes smaller and smaller. *e.g.* $S_{1,2} = 0.5$ (a 50% decrease) but $S_{34,35} \approx 0.9714$ (a 2.86% decrease). So already one can see how higher-order resonances require far smaller perturbation to the layer dimensions to be shifted to the adjacent resonance. This clearly has repercussions here with respect to fabrication tolerances and diameter control during fibre drawing and is discussed in detail below.

Material dispersion can also be incorporated into this resonance scaling analysis. If one uses numerical root-finding of the Sellmeier-based resonance equation, Eq. 5.2, one need only consider the resonance orders as just discussed since the material dispersion is incorporated into the equation by default. However, it is useful to formulate an analytical treatment to make the analysis more intuitive. The task here, then, is to take the pre-calculated roots of Eq. 5.2 and then calculate the scale-shifted resonance wavelengths using only the analytic resonance condition, Eq. 2.4, by incorporating the material dispersion by hand. This can only be done when shifting between resonances calculated in the initial numerical root-finding since they are the only points for which the precise refractive index has already been calculated (shifting to an unknown resonance requires knowledge of the refractive index at that new wavelength which thus requires the root-finding technique, obviating the use of an analytical analysis).

Assume a set of resonances have been calculated by numerically calculating the roots of Eq. 5.2, such as the results in Table 5.4, producing a set of resonance orders, wavelengths and (Sellmeier) refractive indices. By incorporating material dispersion in this way, one must consider that $\Delta n = \sqrt{n_1^2 - n_0^2}$ has a wavelength dependence via $n_1 = n_1(\lambda)$; this would be the F2 glass Sellmeier dispersion relation of Table 5.3 for the case here, so that $n_1 = n_{\mathrm{F2}}(\lambda)$. When this is the case, $\Delta n(\lambda_m)$ also changes with the layer scale (shifting from resonance m to l) as $\Delta n(\lambda_m) \rightarrow \Delta n(\lambda_l)$. The initial resonance is $\lambda_m = 2t_1\Delta n(\lambda_m)/m$ and the other known resonance to which λ_m is to be shifted is $\lambda_l = 2t_1\Delta n(\lambda_l)/l$. By scaling the layer thickness t_1 by a factor $S_{m,l}$, the m^{th} resonance is shifted to the l^{th} only when the $t_1 \rightarrow \frac{m}{l}\frac{\Delta n(\lambda_l)}{\Delta n(\lambda_m)} = S_{m,l}t_1$, as can be confirmed by substituting directly into the form of λ_m. This implies $S_{m,l} = \frac{m}{l}\frac{\Delta n(\lambda_l)}{\Delta n(\lambda_m)}$.

As mentioned earlier, scale-based resonance shifts are critical in the presence of fibre fabrication instabilities. The scale of the fabricated fibres considered here exhibited a $\approx \pm 1\%$ diameter variation during drawing, occurring over length scales of ~ 10 cm. It is thus critical to determine how such structural variations affect guidance. The worst case scenario for observation of antiresonant transmission peaks would be the shifting of resonances over the length of the fibre, due to scale fluctuations, such that the antiresonance conditions ($m = \frac{1}{2}, \frac{3}{2}, \ldots$) of one part of the fibre overlap with the resonance conditions of another ($m = 1, 2, \ldots$). In this case, later sections of the fibre would filter

out the transmission peaks of the earlier sections, flattening out the transmission spectrum. To get a feel for the extent to which this may occur in the fibres considered here, using the methods above one can calculate the scaling factors required to achieve this resonance/antiresonance overlap condition. Since the antiresonance conditions for the fibres of interest have already been calculated in Table 5.4, for convenience the condition for shifting those antiresonances one order up ($\overline{m} \rightarrow \overline{m}+1$) will be considered rather than shifting them by half an order as just discussed (avoiding the need to calculate the associated resonances and their Sellmeier-based refractive indices). The resonance/antiresonance overlap will thus occur for approximately half of the calculated scale factor (up to material dispersion).

Table 5.4 shows the scale factors required, $S_{\overline{m},\overline{m}+1}$, in order to shift the calculated antiresonance wavelengths up by one order. The listed quantity is the percentage by which t_1 must decrease in order to shift the resonance to the next order: $S^{\%}_{\overline{m},\overline{m}+1} = (1 - S_{\overline{m},\overline{m}+1}) \times 100$. It is the case that for both Fibre D_a and E that the required shift becomes less and less for increasing antiresonance orders. This behaviour is dominated by the $m/l = m/(m+1)$ factor as discussed earlier for the case ignoring material dispersion (the inclusion of dispersion typically alters the scale percentage in the second significant figure here—critical for higher-order resonances). Indeed, the highest observed order of Fibre E, $\overline{m} = 34$, requires only a $\approx 2.7\%$ decrease in inner layer thickness to have its wavelength totally shifted to the next higher order.

This implies that a scaling as small as about half of that, 1.35%, is enough to shift the antiresonance into a resonance. As discussed above, this behaviour would lead to a flattening of the transmission spectrum due to a continuously shifted transmission comb throughout the fibre length. Since the fabrication tolerances of these fibres are $\approx \pm 1\%$, this behaviour should be expected for high-order antiresonance peaks. Indeed, this is precisely the behaviour observed of the transmission and loss spectra in Fig. 5.21, discussed earlier. One can thus make the conclusion that the fabrication of such fibres with thick rings, producing very high-order resonances, will easily succumb to fabrication tolerances and a fluctuation of the structural features, resulting in degradation of the very transmission peaks that are of interest.

In contrast, one can see in the loss spectrum of Fibre D_a (Fig. 5.18) exhibits much more obvious loss dips than Fibre E (Fig. 5.21). In particular, the loss feature with highest visibility[11] for Fibre D_a (at the lowest-order anti-resonance shown on the figure at $\lambda = 654.21$nm—from Table 5.4) is well defined (with an inverted Gaussian appearance) and has a considerable depth of ≈ 125dB/m. The most visible loss feature of Fibre E,

[11] loosely defined here as Peak-to-trough depth of a given dip feature.

on the other hand, has a depth of only ≈ 20dB/m, owing to the overlap of higher-order resonances due to the fabrication tolerances.

Due to the sensitivity of higher-order resonances, their exploitation would be ideal for sensing applications, for example, such as refractive index (via filling the fibre) or strain sensing (by bending or deforming it). This suggests that there may be some merit in the design of these spider-web fibres in order to explicitly exploit higher-order resonances, but this would require some refinement of the fabrication process before their visibility becomes appreciable enough for practical use. However, given the observations of the anomalous highly-visible transmission peaks of the short sample of Fibre E (Fig. 5.20), the effect of the resonances of higher-order core modes might provide an alternative route to such resonance-based sensing applications.

It seems more apparent that the refinement of the fabrication process to produce thinner cladding features, producing well-separated resonances and broader bandwidth and lower loss transmission, is a more meritous endeavor since all of the necessary phenomena (within the restrictions of the current fabrication abilities) have been demonstrated above.

In the following section, the properties of the fabricated 2-ring spider-web fibre are simulated using a FEM technique. This analysis has the ability to explain many of the guidance properties of the fibre and, importantly, is used to show that the inner cladding ring resonance has a dominant effect on the confinement loss, with small perturbations due to the second ring which has a different thickness; this justifies the exclusive use of the inner ring resonances in the above analyses and explains its close agreement with experiment.

5.5 Finite Element Analysis of a Fabricated Fibre Structure

Here some results of a finite element analysis (the FEM as used here is discussed in § 2.3.4) upon the 2-ring spider-web fibre, Fibre E, are presented. As discussed in § 2.3.4, the FEM as implemented in this thesis is able to solve for the (leaky) guided modes of an arbitrary waveguide geometry using the fully-vectorial wave equations (§ A.1), ideal for accommodating the complex fibre structures considered above (few other modelling techniques can offer such flexibility with respect to structure and ease of use while maintaining precise and relatively fast calculations). In modelling the fabricated structure here, properties of the waveguide can be numerically investigated in ways inaccessible to other modelling techniques (such as the more simple antiresonance analysis above).

In particular, the effect of the inclusion of struts and surface-tension-induced deformations to the fibre structure will be investigated and compared to the equivalent modes of an idealised equivalent structure (perfect concentric rings). It will also be demonstrated that the model predicts the existence of discernible resonances in spite of the large struts of the cladding structure, in accordance with observations from experiment.

Fibre E was considered for the FEM analysis since Fibre D_a has a more complex structure and finer spectral detail. The complex structure requires a fine FEM mesh to resolve sufficient detail to produce a stable numerical result which requires a significant amount of computer memory, placing a limit on the memory require by the computer used and the minimum amount of time required per iteration of the calculation (a prohibitive amount in this case). The fine detail seen in the experimental transmission spectrum above would require many fine steps in wavelength to resolve when trying to calculate a numerical comparison; coupled with a relatively long calculation time per iteration, a single mode spectrum can potentially take months to complete. Since the analysis here is somewhat preliminary, just providing an insight into some of the fundamental modal behaviours of the full waveguide structure, such calculation times as prohibitive. The transmission and loss spectra of Fibre E above (Figs. 5.20 and 5.21) have a relatively regular appearance with well-defined peaks undulating across the spectrum, rather than peaks amidst fine detail as for Fibre D_a. One can thus get away with the use of larger steps in the spectral FEM calculations since the spectral features would be expected to reveal themselves more readily.

A geometry approximating the glass-air boundaries of the SEM of Fibre E (Figs. 5.14 and 5.19) was generated. Because the glass/air boundary of the SEM image is inherently 'blurred', the definition of this boundary is somewhat arbitrary up to the spatial measurement precision of the SEM, taken to be ≈ 0.2 μm here. This boundary is thus essentially a contour residing at a greyscale value mid-way between the black of the air regions and the grey of the glass. Issues with SEM resolution dictating the precision to which a numerical model geometry can be based are well known, especially with respect to FEM techniques [189]. Nonetheless, the general features are primarily of interest here, rather than precise descriptions of modal spectra. Certainly, in light of the knowledge that the $\approx \pm 1\%$ fabrication tolerances discussed above can have a significant effect on the guidance properties, the ± 0.2 μm ($\approx \pm 3\%$ of Fibre 3's average ring thicknesses) measurement uncertainty becomes less of a concern. In other words, by basing the analysis on the geometrical parameters of the SEM, the guidance properties of a segment of fibre lying within the fabrication tolerances is sufficient for consideration here.

Figure 5.22 (top-left) shows a constructed geometry consisting completely of circular boundary sections and (fewer) linear segments, configured to approximate the SEM

derived geometry of Fig. 5.14 (left) just discussed. The core and rings are concentric circles. The rounded edges of the cladding holes are circular segments whose radii of curvature sum to a value equal to or less than the thickness of the particular air layer. The struts are defined by rectangles whose edges coincide with the apexes of the edge circles. The geometry parameters were tuned by hand so as to closely match the SEM-derived contour geometry. The final parameters used were: $D_{\text{core}} = 40.9145$ μm, $t_{\text{ring,glass}} = 6.25$ μm, 5.481 μm, $t_{\text{ring,air}} = 11.94$ μm, 16.96 μm, $t_{\text{strut}} = 6.3145$ μm.3.3 μm, $r_{\text{hole,1}} = 55\%, 25\%$ of $t_{\text{ring,air}}$, $r_{\text{hole,2}} = 65\%, 35\%$ of $t_{\text{ring,air}}$, $r_{\text{PML}} = 145$ μm (inner radius of PML), $t_{\text{PML}} = 1$ μm. Double values refer first to the inner then outer quantities. $r_{\text{hole,i}}$ refer to the radii of curvature of the corners of the holes (innermost, outermost) as a fraction of the associated air layer ($i = 1$—inner, $i = 2$—outer).

In constructing this cross-sectional structure from geometrical shapes, it exhibits a 16-fold symmetry (8 rotation and 1 mirror), meaning it belongs to the $C_{8,\nu}$ symmetry group [184]. Due to the symmetry of the constructed geometry, one can truncate the domain to a 1/16 azimuthal slice. Owing to group theoretical arguments, this truncated domain can be used to simulate modes for which the boundary conditions support a given mode [184, 185]. Only the TE and TM modes can be modelled using the $1/16^{\text{th}}$ fundamental slice, since hybrid modes require at least a quarter-plane domain in order to induce electric *and* magnetic boundary conditions on the internal domain boundaries (one electric and one magnetic). The smaller domain considered here can be used to solve for TE modes by setting all domain boundaries to electric conductors and the TM modes by setting all boundaries to the equivalent magnetic condition [184, 185].

Beyond enforcing boundary conditions upon the internal domain boundaries, the region external to the waveguide structure must be truncated appropriately. As discussed in § 2.3.4, the termination of the exterior of a solution domain using perfectly matched layers is a means of approximating a surrounding homogeneous medium of infinite extent. The PML itself is incorporated into the FEM calculation as an artificial inhomogeneous, anisotropic, absorbing medium. This requires a tensorial description of the artificial permittivity of the medium such that field lines approaching from any direction and of any amplitude are attenuated in a similar manner. The PML formulation used here is discussed in detail in Refs. [182, 187].

By truncating the solution domain using the symmetry and absorbing PML techniques just described, the number of mesh elements required in order to discretise the geometry and solve for the appropriate eigenmodes is greatly reduced. Indeed, the calculation wouldn't be at all possible without the inclusion of an absorbing PML boundary domain (reducing the effectively infinite cladding region to a finite one). The exploitation of the

symmetry of the structure and supported modes allows a further reduction in the required number of mesh elements (by a factor of 16 here). Each vertex (node) and edge of a mesh element represents a set of field amplitudes and phases which, in aggregate across the entire mesh, form the characteristic discretised matrix of the waveguide system [183]; the fewer mesh elements required, the more efficient the calculation in terms of requires memory and computational power. Indeed, without truncating the domain to this extent, the following calculations would be prohibitive, requiring greater computational resources than readily available to me at the time of research. As for all FEM calculations within this thesis, the commercial FEM package COMSOL Multiphysics [182] is employed.

Fig. 5.22 shows the reduced domain with an example of a generated discretisation mesh using COMSOL's advanced mesh generation routines. The maximum average mesh element edge sizes for each domain are: core—0.5 μm, glass structure—0.15 μm, PML—0.05 μm. The air-holes are meshed using a preset automatic growth factor, reaching a maximum element size in their centre of about the same as the core. These mesh parameters result in the generation of approximately $100,000$ mesh elements in total, using between 5 GB to 10 GB of system RAM with each iteration taking approximately 10 minutes (requiring a total calculation time of over a week for the spectra calculated here).

As for previous sections above, the Sellmeier form of the glass refractive index is used in all FEM calculations here. *i.e.* an accurate material dispersion description is used making the refractive index wavelength dependent as per Table 5.3.

First, an idealised version of the geometry is modelled. As done in Chapter 2, one ignores the struts of the geometry such that all that remains are perfect concentric rings. All other parameters are kept the same as those defined for the realistic geometry above, sans connective struts.

Figure 5.23 shows the calculated $\tilde{n}$ and CL for the TE_{01} and TM_{01} modes over a wavelength range of $\lambda = 0.5$ μm $\rightarrow$ 0.6 μm. This range is covered by the experimental transmission spectrum data for Fibre E in Figs. 5.20 and 5.21. In order to sample out these modes from all solutions found, only modes with an integrated Poynting vector ($\mathbf{S}$) z-component S_z in the core greater than 75% of the total modal power, and values of $\tilde{n} > 0.9997$, were considered. The integral measure of S_z is a mode's so-called *power fraction* in the core and is expressed as: $P_{\text{core}} = \int_{\text{core}} S_z dr d\theta / \int_{\text{domain}} S_z dr d\theta$ where $\mathbf{S} = \mathbf{E} \times \mathbf{H}$ and $S_z = \mathbf{S} \cdot \hat{\mathbf{z}}$.

One can immediately see in Fig. 5.23 how the anti-crossings (discontinuities) present in the effective index spectrum approximately coincide with the resonances of the inner

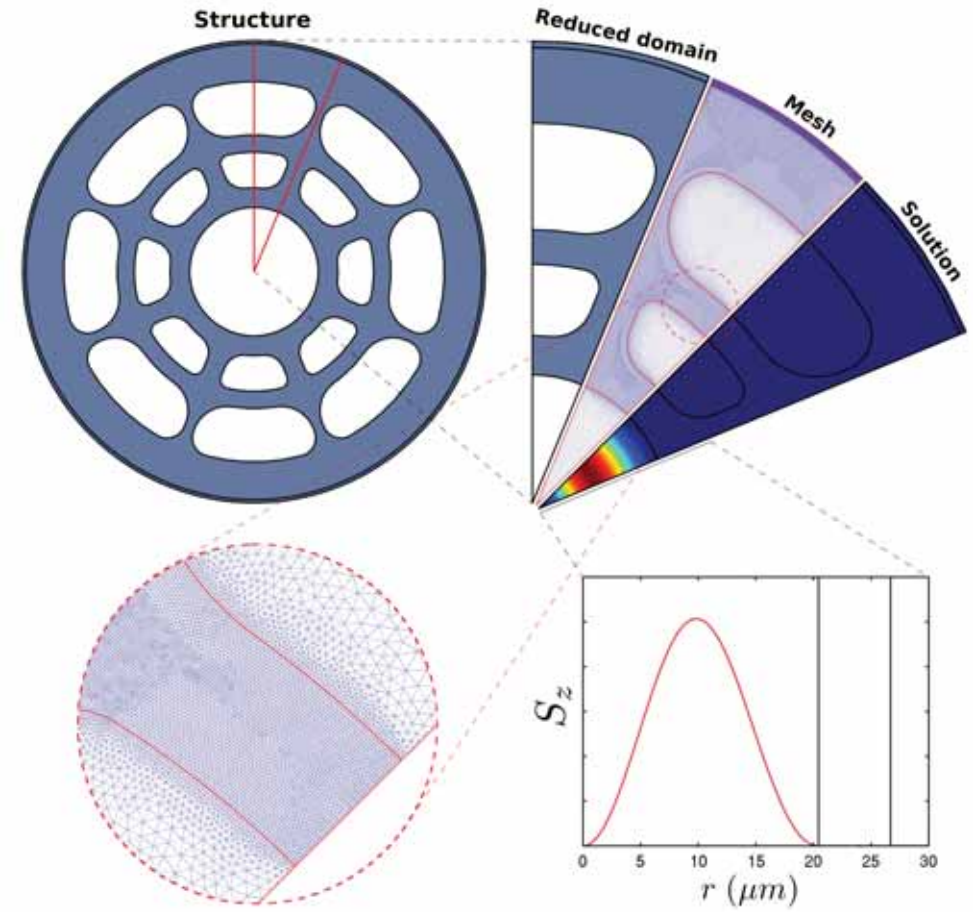

FIGURE 5.22: *Top-left:* Full geometrical reconstruction of the cross-sectional microstructure of Fibre E. Dark regions: glass. White regions: air. The thin annulus around the edge of the structure represents the PML. Structural and material parameters used in the model are discussed in the text. *Top-right:* Representations of the three primary stages of the FEM calculation: truncation of the full geometry to a minimal sector ($1/16^{\text{th}}$ angular segment), distribution of the generated finite element mesh upon the truncated geometry, an example of a solution of the model (S_z of the TE_{01} mode at $\lambda = 543.5$ nm). *Bottom-left:* Zoom-in of the mesh. *Bottom-right:* A slice of the shown S_z surface.

ring for both mode types. This is almost identical to the band-edge behaviour of the guided modes calculated in Chapter 2 for a similar idealised geometry; for that case, though, all rings were of equal thickness. Also similar to the Chapter 2 case is the fact that the edges of the TM discontinuities occur further from the resonance than for the TE, likely due to an analogous Brewster effect as discussed at length in the chapter. The important point to note here is that the current behaviour occurs in spite of the fact that the second ring has a significantly different thickness, producing resonances generally far offset (Fig. 5.23, bottom) from those of the inner ring.

This is in agreement with much of the observed behaviour in experiment for both Fibre E

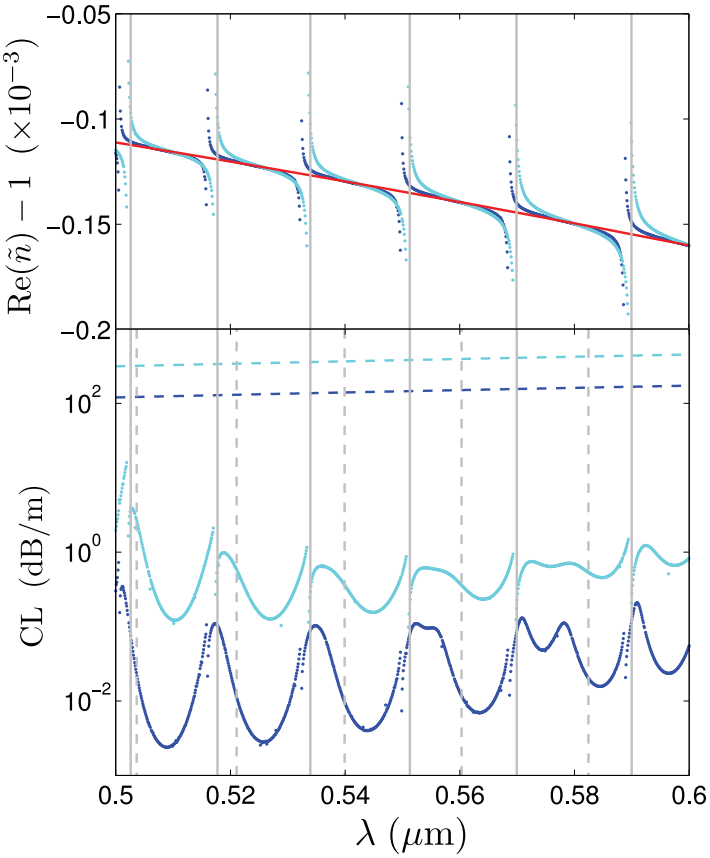

FIGURE 5.23: FEM calculations of $\mathrm{Re}(\tilde{n})$ and CL TE_{01} and TM_{01} mode spectra of an idealised model of Fibre E. *Blue points:* TE_{01} mode. *Cyan points:* TM_{01} mode. *Red curve:* $\mathrm{Re}(\tilde{n})$ of the equivalent tube guide (TE and TM are degenerate). *Dashed curves:* CL of the equivalent tube guide modes; *blue*, TE_{01}; *cyan*, TM_{01}. *Vertical grey lines:* resonance wavelengths λ_m of the inner (*solid*) and outer (*dashed*) glass rings.

and Fibre $\mathrm{D_a}$ where the transmission peaks and loss minima coincided with the inner-layer resonances. As argued there, this behaviour is predominantly because the guided mode field has a greater amplitude at the interface of the first ring than the second, due to it decaying into the structure; this decay is explored explicitly for the realistic geometry presently. Indeed, from the fundamental field-based integral expression for β (Eq. A.26), as light is permitted within a certain cladding features β (or $\tilde{n}$) will be influenced predominantly by those features in which it has the largest field amplitude, as argued in Chapter 2.

The confinement loss calculations shown in Fig. 5.23 are also in agreement with this behaviour, with the high-loss regions approximately coinciding with the inner-ring resonances. While not as convincing as the discontinuities imbued by the inner-ring resonances, the outer-ring resonances (dotted vertical grey lines) do seem to influence the CL spectra of both modes. Indeed, the CL curves appear to become warped, as if they are influenced by a loss feature; indeed, this loss feature is likely the coupling to the

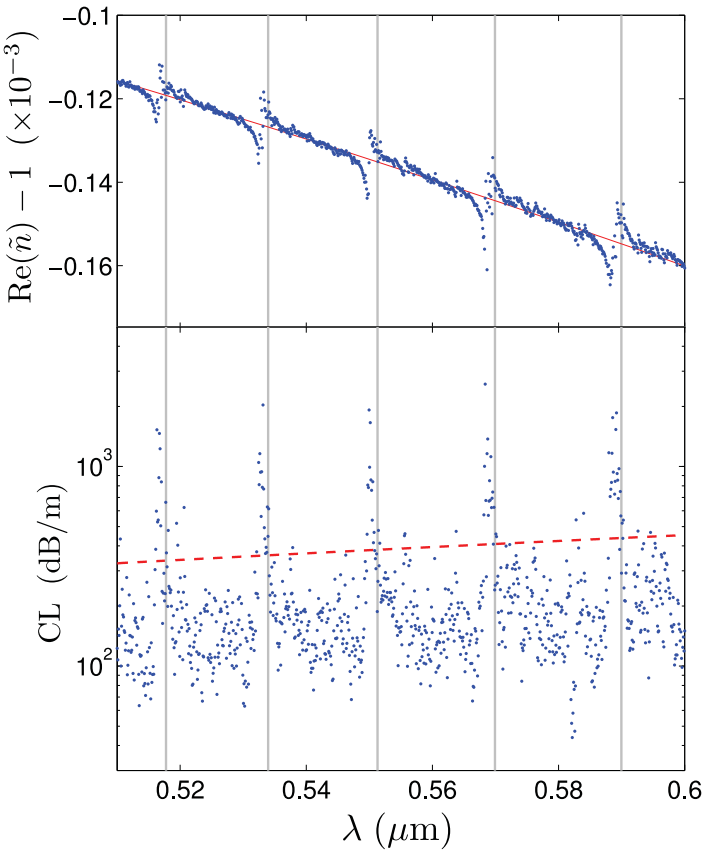

FIGURE 5.24: FEM calculations of $\mathrm{Re}(\tilde{n})$ and CL of the TE_{01} mode of a realistic model of Fibre E. *Red curve:* $\mathrm{Re}(\tilde{n})$ of the equivalent tube guide. *Dashed curve:* CL of the equivalent tube guide mode. *Vertical grey lines:* resonance wavelengths λ_m of the inner glass ring.

second cladding layer close to its resonance. In line with this reasoning, the effect is strongest when the outer-layer resonances sit closest to the middle of adjacent inner-layer resonances. Of note is that the TM mode appears to adopt a similar shape to the TE, but at the expected larger loss value. Nonetheless, the loss values themselves don't appear to be influenced too severely, the CL remaining a few order of magnitude below the equivalent tube mode CL curves.

Note the fact that while the inner-ring resonances predict the high-loss regions of the fibre both in theory and experiment, they do not explain the anomalous (but highly regular and visible) transmission peaks of the short length sample of Fibre E shown in Fig. 5.20 and Fig. 5.21. As per the argument above, these anomalous peaks are likely the result of the cumulative effect of higher-order modes that aren't appreciably attenuated over the short length and that potentially don't satisfy the same resonance conditions as the lower order modes for this fabricated structure. This warrants further investigation by simulating such higher order modes with the FEM as for the low-order modes here.

The realistic geometry is now considered. Figure 5.24 shows the calculated $\tilde{n}$ and CL for the TE_{01} mode over a wavelength range of $\lambda = 0.51\ \mu\text{m} \rightarrow 0.6\ \mu\text{m}$. Immediately obvious is that the mode trajectory is no longer 'smooth' but consists of many points apparently locally scattered about a common curve. The reason for this becomes more apparent when one takes a closer look at the modal fields themselves.

Figure 5.25 shows the longitudinal and radial Poynting vector components $S_z = \mathbf{S} \cdot \hat{z}$ and $S_r = \mathbf{S} \cdot \hat{r}$, respectively, over the computation domain. The mode is sampled at a wavelength of $\lambda = 543.5$ nm which is close to an antiresonance of the inner ring. The normalisation constant used is the total axial power over the full computation domain: $S_z^{\text{tot.}} = \int S_z(r, \theta) dr d\theta$. Since arbitrary units are sufficient here, this normalisation isn't strictly required, but was used in the plotted quantities, nonetheless. The logarithm of these quantities is taken in order to reveal the small-amplitude detail that is otherwise visually imperceptible; for example, the solution surface plot shown in Fig. 5.22 is a linear representation of S_z—only the core power is apparent since the field amplitudes in the core are so large compared to those of the cladding which appear to be almost uniformly zero on the linear scale. However, Figure 5.25 shows how the cladding fields and power certainly are not null and exhibit an incredibly rich variety of features which are and vitally important for the understanding of the guidance properties at play.

Of particular note is the 'speckled' nature of the mode intensity in the high-index (glass) cladding regions. This can be thought of as the result of complex scatterings and interference off of the various cladding features (rings, struts, rounded corners, etc.); in the same way one can employ a wave interference technique in describing the origin of conventional waveguide modes, a more complicated, non-uniform, waveguide structure produces nontrivial mode patterns. This speckle pattern shifts rapidly with changing wavelength. It should be noted that the mesh parameters used for the spectra calculations here do not fully resolve this speckle pattern; the features described here are the result of observing solutions manually (one by one) with increased mesh parameters that can resolve the pattern sufficiently (which takes a much longer time to calculate). Fully resolved or not, the waveguide behaviour discussed here is observed to be similar. With this rapid local fluctuation of the modal fields, cumulative properties of the mode such as $\tilde{n}$ and CL will also naturally fluctuate. The scattered nature of the data points just mentioned is a result of complex interference interplay[12]. Nonetheless, it is apparent that these fluctuations do not destroy the general trends exhibited by $\tilde{n}$ and CL as shown in Fig. 5.24. This rapid fluctuation (in CL at least) was observed in the CL

[12]Surface-mode type interactions may also be at play, manifest due to the broken symmetry that the struts provide and the rich variety of potential cladding modes (created by this speckle effect) with which to create anti-crossings. The resonance-based argument for the fluctuations is more likely, however, given that no obvious anti-crossing events were observed between the resonances for the simulations discussed (although a thorough investigation was not performed).

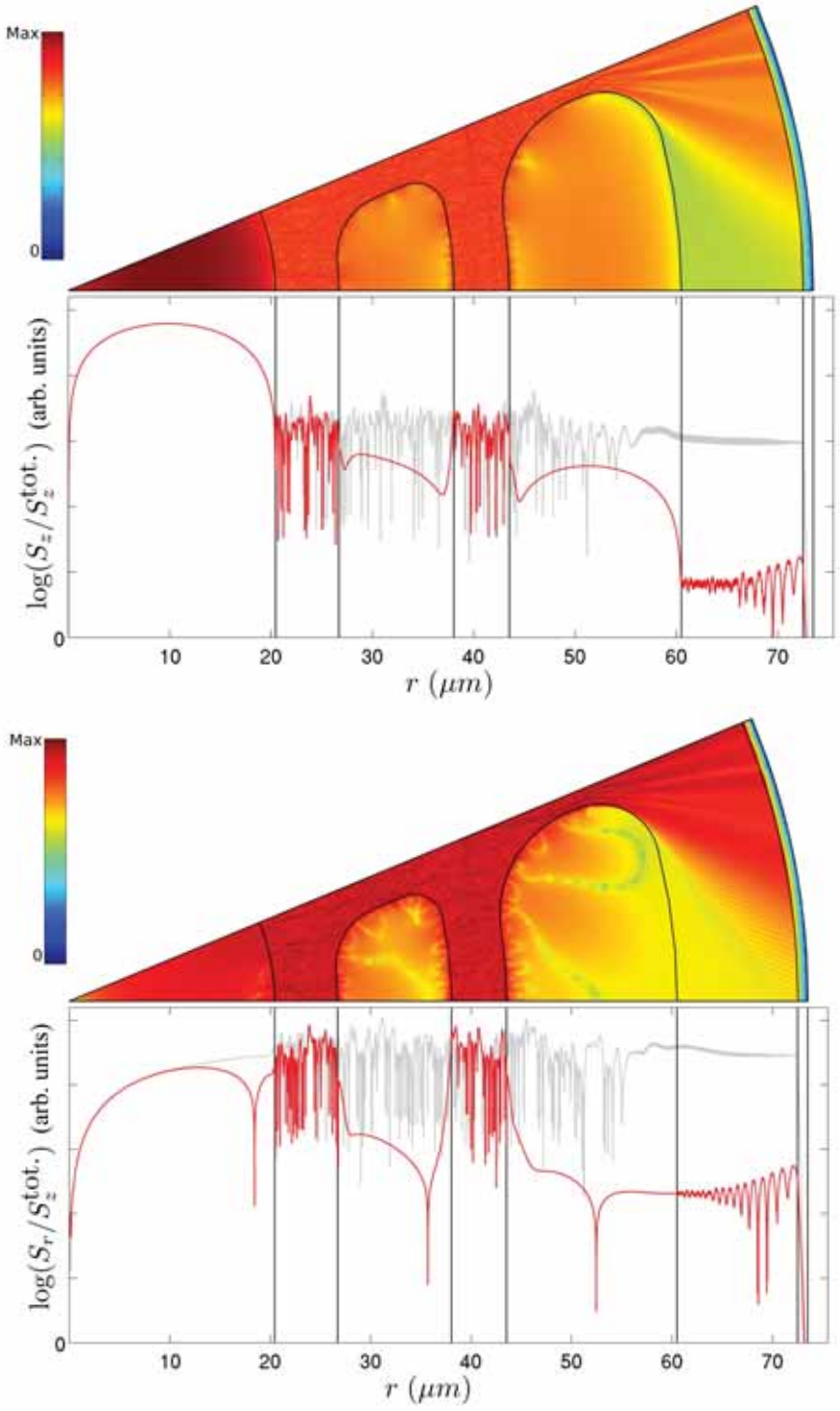

FIGURE 5.25: FEM calculation of normalised longitudinal ($S_z/S_z^{\text{tot.}}$, *top*) and radial ($S_r/S_z^{\text{tot.}}$, *bottom*) time-average Poynting vector components (axial and radial power flow) for the TE_{01} mode of Fibre E at $\lambda = 543.5$ nm. *Red curve:* linear data slice from the centre of the core region along the domain edge intersecting the air holes and rings. *Grey curve:* similar linear data slice but along the opposing edge which passes through the centre of the strut. *Black lines:* the interfaces between glass and air (edges of the rings and struts).

calculations for the spider-web type hexagonal ring structure in § 2.7.2 (Fig. 2.12) and also observed in similar FEM calculations for hollow-core Kagomé fibre structures [145], so its emergence here is not too surprising owing to the similarities between the structures as argued earlier. Given the apparent generality of this speckle phenomenon to (at least) VNW guiding waveguides, there is ample justification for further study on its origins and implications.

It will be noted that these rapid fluctuations do not appear in the measured transmission or loss spectra of the fabricated fibres (also discussed in § 2.7.2). This can qualitatively be explained by arguments of fabrication tolerances. Since the structural dimensions naturally fluctuate during the fibre drawing process, as discussed at length above, these rapid fluctuations would significantly overlap over a given practical length. Just as for the arguments above relating to the 'washing out' of resonance features due to overlapping resonances, the overlapping of these rapid fluctuations would have the effect of smoothing out their appearance. Indeed, this is precisely the effect considered in Ref. [154] in which a convolution method was employed to accommodate for the smoothing effect of structural fluctuations on the modal dispersion of chirped-cladding HC-MOFs [13]. Also, these rapid fluctuations have been observed in the numerical calculations of Ref. [145], for example, and yet, as here, the experimental results of the equivalent fabricated fibre (*e.g.*, Ref. [9]) indicate a relatively smooth transmission and loss spectrum (assuming that sufficient spectral resolution has been achieved during the measurements).

Just as for the Kagomé structure calculations of Ref. [145], the scattered points of the CL calculations still appear to adhere to a general trend reminiscent of the idealised equivalent geometry's behaviour. As the resonances of the inner-ring are approached, the loss of the guided mode increases dramatically. This implies that in spite of the complex nature of the guided light within the realistic cladding structure, the resonances of the rings still play a dominant role. This observation is mirrored in all experimental results shown above and is a critical observation for this research.

Indeed, a natural corollary of this is that the concept of antiresonance appears to survive for the realistic geometry case too since the CL spectra appear to reach a (somewhat stochastic) local minimum mid-way between the resonance wavelengths. Given this strong relationship in experiment and theory to the behaviour of waveguides such as the Kagomé fibre (as discussed numerous times throughout this thesis, *e.g*, §§ 1.4 and 2.7.2) it is most likely that the spider-web fibres here guide via a Von Neumann Wigner guidance mechanism which allows the existence of an antiresonance confinement mechanism in the midst of an effective continuum of cladding modes.

[13] Although, as mentioned in § 1.2.3, it was not explained how or why the structural convolution technique of Ref. [154] works, except that it produced numerical results closer to experiment than the untreated data.

Another critical result of the power distributions shown in Fig. 5.25 is the effect of the rings and struts on the guided light. The curves below the surface plots represent slices of the surface data along one or other of the two primary domain edges. The data is sampled from the centre of the core region along the domain edge. The red curve corresponds to the edge intersecting the air holes and rings. The light grey curve corresponds to the edge intersecting the centre of the strut. As for the idealised case of Chapter 2, the rings (or more precisely, the air gaps between the rings) clearly allow the mode field to decay rapidly as it propagates away from the core area. This is critical for the reduction of confinement loss since the integrated amplitude of S_r across the boundary is a direct measure of the confinement loss itself, as per Eq. A.27; the lower the power at the boundary, the lower the confinement loss.

Thus, one can immediately see why the calculated confinement loss of the realistic geometry is so much higher than that of the idealised geometry (the latter had CL a few orders of magnitude below that of the equivalent tube, Fig. 5.23, but the former had a minimum CL less than one order below the equivalent tube's, Fig. 5.23). The reason lies in the fact that the struts are, perhaps unsurprisingly, very efficient at outcoupling the light from the core, almost as waveguides in their own right. This is seen in the fact that, as shown in Fig. 5.25, the radial and longitudinal power fluxes along the strut are much higher than those through the rings. Indeed, the strut appears to maintain a steady outgoing power flux amplitude along its length until it emerges into the jacket whereupon the light diffracts rapidly into jet-like features, reaching the domain boundary at a very high level. Nonetheless, as discussed, the antiresonance effects and exponential decay within the air regions between the rings sees the power flux drop rapidly across the rings, providing the only mechanism capable of reducing the loss below that of a simple tube.

A sensible conclusion from this would thus be that a reduction of strut thickness would naturally decrease the CL of the waveguide. Preliminary calculations (not presented) suggest that the resultant phenomenology due to altering the strut thickness (or hole radii of curvature) is nontrivial, but is nonetheless a logical step in the direction to refining the design of these spider-web HC-MOF designs. Since thinner rings are also required in order to reduce CL and widen the transmission bands, as discussed, the next obstacle in fabrication is to reduce the minimum fabricable feature size. This was a goal at the outset of the fabrication designs and trials and requires refinement of both the extrusion and, more importantly, fibre drawing techniques (inflation in particular). The extrusion technique is already capable of producing high-quality preforms, so given the success of other silica- and polymer-based fibres such as the Kagomé- and square-lattice fibres discussed in Chapter 1, it seems likely that these goals of fabrication procedure refinement are within reach; namely, the inflation of the structure to produce large

cladding pitch and large air-filling fraction fibres with thin struts and rings down to the target thicknesses of ≈ 300 nm. If met, such spider-web structures could produce broad transmission spectra over the visible and near-infrared, with a view to extend into the mid-infrared, with all of the benefits of the flexible spider-web geometry and its guidance properties discussed throughout.

5.6 Concluding Remarks

The design, fabrication and simulation of soft-glass hollow-core microstructured optical has been presented.

The cross-sectional structure of the HC-MOFs was ultimately based on a spider-web design in which the cladding consists of concentric polygonal rings that are supported by colinear connective struts at there apexes. This design was arrived at after fabrication trials utilising offset struts exhibited significant surface-tension effects, distorting the target structure (§ 5.3.1). The colinear nature of the struts of the spider-web design works with the surface tension to produce fibre structures that naturally maintain their structural integrity during fabrication (§ 5.3.2).

Preforms, which are subsequently drawn down to fibre (§ 5.2.2), were fabricated via an extrusion process in which a bulk soft-glass billet is heated up to its transition temperature, softening it, allowing it to be pushed through a structured die (§ 5.2.1). Upon exiting the structured end-face of the die and cooling, the glass forms the solid preform structure. Extrusion is a vital component to the fabrication process since its flexibility is amenable to the unique structural requirements of the for spider-web fibres that would make them difficult to fabricate by other preform fabrication methods such as capillary stacking, drilling, or casting.

The guidance properties of the fabricated fibres were demonstrated experimentally (§ 5.4). Multiple transmission peaks were observed in the visible to near infra-red spectrum both considered fibres. Transmission losses of the fibres was measured using a cut-back technique. The regions of high loss for both fibres were shown to correspond to the wavelengths satisfying the resonance conditions of the inner cladding ring; with the low-loss regions generally satisfying the anti-resonance conditions. Material dispersion of the lead-silicate glass used had to be considered in the resonance calculations in order to achieve a close agreement between the calculations and the experimental results.

Extending the antiresonance analysis, it was shown that the structural fluctuations during the fibre drawing process are likely responsible for the reduction in discrimination between the high and low loss features of the demonstrated 2-ring spider-web fibre,

resulting in a 'flattening out' of the transmission and loss spectra towards lower wavelengths. The predominance of this effect for the 2-ring fibre compared to the other, 4-ring, version, was shown to be due to the fact that the rings of the 2-ring version were much thicker and thus exhibited much higher-order resonances in the measured spectral region. It was quantitatively demonstrated how higher-order resonances are more sensitive to structural fluctuations and hence more susceptible to overlapping each other (§ 5.4.2), washing out their appearance in the measured transmission spectra due to the cumulative losses of the overlapping resonances. The effect upon the 4-ring fibre was less pronounced due to the fact that it exhibited thinner rings, hence lower-order resonances that are less sensitive to perturbations.

The modal properties of the fabricated 2-ring fibre were analysed via a numerical finite-element method (§ 5.5). For both idealised and, importantly, realistic structural representations of the fibre structure, the resonances of the inner ring were found to produce the dominant effect on the confinement loss spectrum. This is an important observation since the second cladding ring has a different thickness and hence supports resonances at different wavelengths. These results are in accordance with that observed from experiment and represent a validation for considering only the resonances of the inner ring in the antiresonance analyses. The second ring was found to only have a more subtle effect on the shape of the CL spectra, with the inner ring producing the strongest resonance features (Fig. 5.23), as would be expected due to the guided fields having greatest intensity at the inner ring.

These results highlight that the spider-web HC-MOF design certainly behaves as is expected from theory, demonstrating that they have the potential to adopt the best features of air-Bragg and Kagomé fibres. however, in order to increase the transmission bandwidth and lower the losses of these fibres, further research is required into the means of decreasing the minimum structural feature sizes down to the target thickness of ≈ 300 nm, presumably via an inflation technique during the drawing process. Active inflation attempts were attempted and reported above (§ 5.3.2, Fig. 5.12), but the poor structural fidelity indicates the technique requires refinement, possibly via differential pressurisation of the various cladding hole types or by employing a larger draw-down ratio under a self-pressurisation mechanism.

If these fabrication obstacles can be overcome, spider-web HC-MOFs could produce broad transmission spectra over the visible and near-infrared, with a view to extend into the mid-infrared, with all of the benefits of the flexible spider-web geometry and its guidance properties discussed throughout.

Chapter 6

Conclusion and Future Work

Waveguidance in media with a low refractive index can be challenging due to the propensity for light to seek regions of higher index. Coercing light to be guided within a region of low index is nontrivial and can be approached using a number of various waveguidance phenomena and waveguide designs.

The work within this Thesis was related to two primary themes:

- The fabrication, analysis and simulation of single-material hollow-core microstructured optical fibres made from soft-glass via an extrusion process;
  Chapters 2 and 5.
- The guidance behaviour of binary–layered-cladding waveguides with cores of arbitrary refractive index equal to or less than the lowest of the cladding;
  Chapters 2, 3 and 4.

The first theme, regarding soft-glass hollow-core fibres, was the initial motivation of this research: there was little literature on hollow-core guidance within optical fibres made from soft-glasses, and no reports of the fabrication and demonstrated guidance of such a fibre. Such fibres hold great promise for applications to mid-IR guidance, high-power delivery, nonlinear optics and sensing, as well as novel properties for the conventional shorter wavelength spectrum. Today, while this gap in the suite of reported fibre architectures still exists, there have been numerous theoretical, fabrication and experimental works reporting progress, but none detailing the successful fabrication and demonstration of a soft-glass hollow-core optical fibre.

The findings presented in Chapter 5 detail the successful and novel fabrication of such fibres using an extrusion preform fabrication process. By exploiting the guidance mechanisms and principles discussed in the literature, and summarised in the Introduction, the fibre's cross-sectional microstructure design was akin to a spider-web: concentric polygonal rings supported by colinear radial struts - a geometry that works with the natural surface tension effects of the glass during fabrication to produce considerable structural fidelity. The fabrication of this novel structure is currently unique to, and

ideally suited to, the extrusion method. It was demonstrated how the fabricated fibres indeed guided by an antiresonance effect in the absence of full cladding bandgaps, akin to the Von Neumann Wigner guidance mechanism.

While these results constitute a proof of principle of the suitability of the fibre design, further work is required to refine it in order to reduce the confinement losses and control the guidance properties. Most importantly, a means of increasing the air-filling fraction of the structure is critical to broadening and lowering the loss of the core-guidance wavelength ranges. While self-inflation appears to be the ideal means of inflating this structure, it is limited by the size of the preform itself and the apparatus used to produce and draw it. The alternative, active inflation, resembles a significant obstacle due to the variable inflation of the differently sized cladding holes, warranting investigation into more complex inflation techniques, such as variable and controlled pressure for individual cladding holes during the drawing process.

If such obstacles can be overcome, the spider-web design via the extrusion method represents a way towards the fabrication of low loss hollow-core microstructured fibres fabricable in a variety of extrudable glasses, from silicates to chalcogenides. In fact, a simplified version of the structure, having only one cladding ring, has been demonstrated in silica [149] and would be an ideal structure to initially investigate for such future work since the antiresonance guidance mechanism would still be substantial but with a more simple structure. There is also a potential wealth of theoretical insights to be discovered about the guidance behaviour and mechanisms of such fibres, with some findings reported in §§ 2.7, 5.4 and 5.5 that demonstrate and discuss novel guidance phenomena.

In reviewing the literature in order to determine the best approach to achieve the above goal of a guiding soft-glass hollow-core fibre, it became obvious that there was a large array of different guidance mechanisms and waveguide structures that exploit them. The Introduction presents a thorough review of these mechanisms and structures together with a discussion of their relationships, similarities and differences. It became apparent that there were still significant areas that weren't connected in the literature. This lead to the discovery that the antiresonance and bandgap mechanisms in binary-layered optical structures have a deep connection (Chapter 3).

These findings ultimately led to the investigation of the second theme above, regarding binary-layered cladding low-index core waveguides. This theme was identified as a complementary avenue of research while investigating the guidance properties of air-Bragg fibres (closely related to the final spider-web design here). Chapter 2 demonstrated how higher-order bandgap along the low-index light-line could produce core-mode confinement losses much lower than those achievable by simply scaling the core diameter. During this research, the discovery of a nontrivial, but somewhat regular, topology of

bandgaps below the low-index light-line of a silica air-Bragg fibre suggested that there was a rich physical insight to be had in explaining this bandgap structure. To investigate this, the antiresonance/bandgap unification I had found was exploited in order to construct the Stratified Planar Antiresonant Reflecting Optical Waveguide (SPARROW) model, presented in Chapter 3. The SPARROW model is applicable to any binary-layered optical structure and describes the resonances of the layers below the light-line. This chapter also showed that this representation of layer resonances could be used to quantitatively describe nontrivial features of bandgap and reflectance spectra, using completely analytic forms. The SPARROW model is thus a powerful and simple tool for the fundamental analysis and design of binary-layered optical media, in particular layered cladding dielectric waveguides with core refractive indices equal to or less than the lowest cladding index.

Following recent work by Hsueh et al. [202], the relationship between the SPARROW model resonance intersection points and the Bloch bandgap closure points can be shown to be mathematically exact and points a way to further fundamental investigations into the connection between the Bloch theory and (anti)resonance. Also, the novel analyses of Chapter 3, connecting the reflectance response of multilayer structures with the resonance and antiresonance of each layer, are particularly promising given recent findings of Zhang et al. [210] whose work was published in the final month of compiling the final version of this thesis. They demonstrated a simple reflectance-based analysis for a precise approximation to multilayer-cladding confinement loss, obviating the need for complicated numerical models. This suggests promising future work in which the unification of resonance and reflectance phenomena in Chapter 3 are integrated into this simplified confinement loss model, providing both novel insight into the physical mechanisms and also producing a simple means of designing such waveguides.

This lead to the motivation for the experimental investigation of Chapter 4 in which the sub–light-line bandgap spectrum of a Bragg fibre was probed by systematically filling the hollow core with liquids of various refractive indices. The transmission spectrum of the Bragg fibre was observed to shift to shorter wavelengths after as the refractive index of the liquid within the core was increased and different regions of the bandgap spectrum were probed by the shifted effective mode index. Of particular note was that, in order to reasonably compare the experimentally observed transmission spectra with the Bloch bandgap windows, the cladding material dispersion had to be taken into account (rarely considered in the literature and a direct result of the novel nature of the varying core index throughout the wide bandgap spectrum). The particular fibre used had a cladding bandgap spectrum with only a single, fundamental, bandgap within the measured (visible) spectrum; further work would ideally use a fibre with a more complex cladding bandgap structure within the spectrum and core indices of interest

(by fabricating thicker layers, say) which would be more amenable to analysis via the SPARROW model.

Refinement of the experimental procedure is required in order to better understand the interaction of the guided modes with the TE and (particularly) TM bandgap spectra. With the consideration of alternate fibre designs, such sensitivities could be enhanced, making the multilayer liquid-core waveguide a promising architecture for, say, microfluidic refractive index sensing as recently suggested by Skorobogatiy et al. [19].

While the initial intentions for the research towards this thesis were relatively well defined (the fabrication of a guiding soft-glass hollow-core optical fibre), what was discovered was an incredibly rich suite of waveguidance phenomena and their applications to varied waveguide architectures, from optical fibres to on-chip devices. Their understanding and applications are rapidly progressing thanks to a vibrant research community keen to demonstrate and exploit these versatile waveguidance phenomena and the structures made to support them. The work presented in this thesis has gone some small way to advancing this effort, from bringing together fundamental concepts within the initially disparate areas of antiresonance and bandgap waveguide mechanics for 1-D layered media, to the design, fabrication and analysis of novel soft-glass hollow core fibres. I look forward to observing the rapid progress of this field in the time to come, and where possible, to continuing my own small but incremental contributions to it.

K. J. Rowland